

# Lockin Thermography Parameter Investigation

by  
Emmanuel Mutale Bwembya

*Thesis presented in partial fulfilment of the requirements for the degree  
of Master of Engineering (Mechanical) in the Faculty of Engineering at  
Stellenbosch University*



Supervisor: Prof. K. Schreve

March 2017

## Declaration

By submitting this thesis electronically, I declare that the entirety of the work contained therein is my own, original work, that I am the sole author thereof (save to the extent explicitly otherwise stated), that reproduction and publication thereof by Stellenbosch University will not infringe any third party rights and that I have not previously in its entirety or in part submitted it for obtaining any qualification.

Date: March 2017

Copyright © 2017 Stellenbosch University

All rights reserved.

## Abstract

# Lockin Thermography Parameter Investigation

E.M Bwembya

*Department of Mechanical and Mechatronics Engineering,*

*Stellenbosch University,*

*Private bag XI, Matieland 7602, South Africa*

Thesis: MEng (Mech)

March 2017

Infrared thermography has emerged as one of the leading nondestructive testing techniques used for composite materials testing. It is fast, safe, effective and data acquisition is done remotely. As such it has attracted significant research to improve its performance in detection of material flaws in carbon and glass fibre composites.

The aims of this thesis were to investigate parameters that affect defect detectability with optical lockin thermography. These were the frequency, intensity, number of wave cycles of the excitation and material type for which both simulations and experiments were conducted. The materials contrasted were carbon fibre composite and mild steel as they display a large disparity in thermal properties and density.

A major note to make was that the material with lower thermal conductivity and heat capacity produced better results in experimental data while results in simulated data were similar. Low values of thermal effusivity enhanced defect detection and reduced the effect of experimental noise. Furthermore, other results showed that low frequencies probe deeper into the material and as such increase the probability of detecting deep defects. In the case of intensity of thermal excitation, low excitation intensities resulted in a low temperature rise which if too low equalled the camera noise and deterred defect detectability. This was especially so for mild steel which has a high heat capacity. As for the number of wave cycles, increasing this parameter had little influence on increasing the probability of defect detection in simulations as the phase response of the curve was barely altered by using more cycles as there was no noise in simulated data. Experimental results showed improved results for both materials.

## Opsomming

Infrarooi termografie het navore gekom as een van die uitstaande nie-destruktiwe toets tegnieke vir saamgestelde materiale. Dit is vinnig, veilig, effektief en behels geen direkte kontak nie. Daarom is daar 'n beduidende hoeveelheid navorsing na die vermoë van die tegniek om materiaal defekte in koolstof- of glasvesel materiale te identifiseer.

Die doelwitte van hierdie tesis was om die parameters te ondersoek wat die vermoë van optiese vaspen termografie beïnvloed om defekte suksesvol te identifiseer. Dit het ingesluit frekwensie, intensiteit, aantal warmtebron golf siklusse en die materiaal tipe. Beide simulاسies en eksperimente is uitgevoer. Koolstofvesel saamgestelde materiale is met staal gekontrasteer omdat hulle uiteenlopende termiese eienskappe en digthede het.

'n Belangrike bevinding is dat die materiaal met laer termiese geleiding en warmtekapasiteit beter resultate opgelewer het in die eksperimente terwyl die simulاسie resultate soortgelyk is. Lae termiese effusiwiteit verbeter die defek herkenning en verminder die effek van eksperimentele geraas. Verdere resultate toon dat lae frekwensies dieper defekte in die materiaal kan herken en verhoog dus die waarskynlikheid dat defekte herken sal word. Wat die intensiteit van die hittebron betref, veroorsaak lae intensiteite lae temperatuur stygings wat in sekere gevalle gelei het tot stygings wat kleiner was as die kamera resolusie en dus defek herkenning belemmer het. 'n Toename in die aantal hittebron siklusse het nie 'n groot invloed gehad op die waarskynlikheid om defekte in simulاسies te herken nie, want die fase terugvoer van die kurwe was kwalik verander omdat daar geen geraas in die simulاسie data was nie. Eksperimentele data toon verbeterde resultate vir beide materiale.

## Acknowledgements

I would to express my sincere gratitude Prof. Schreve for his guidance, support, knowledge and encouragement.

I sincerely thank Prof. Venter, Prof. Harms, Dr. Venter, Dr. Blaine, Dr. Owen, and Mr. Tshwane for their willingness to assist in areas of their expertise related to the project.

Further, I would sincerely thank Mr. C. Zietsman, Mr. Pitressi, Mr. F. Zietsman, Mr. Stanfielt and Mrs. Galant for their assistance with regards to ensuring equipment and material were available and on time.

I am also grateful to my family and friends for their continued encouragement and motivation throughout the project.

Last but not the least, my colleagues Mr. Oppong, Mr. Azkampo, Ms. Marias, Mr. Jivan, Mr. Wilkinson, Mr. Butler and Mr. Bock for the amazing office atmosphere.

## Dedication

I would like to dedicate this thesis to the Lord Almighty for giving me strength, my family and to the inspired people I met along this Journey.

## Table of Contents

Declaration.....	i
Abstract.....	ii
Opsomming.....	iii
Acknowledgements.....	iv
Dedication.....	v
Table of Contents.....	vi
List of Figures.....	x
List of Tables.....	xiii
Nomenclature.....	xiv
1 Introduction.....	1
1.1 Background.....	1
1.2 Motivation.....	2
1.3 Objectives.....	3
1.4 Thesis Outline.....	3
2 Literature Review.....	4
2.1 Composite Defects.....	4
2.2 Composite Damage.....	5
2.3 Nondestructive Testing Techniques for Composite Materials.....	5
2.3.1 Ultrasonic Testing.....	5
2.3.2 Acoustic Emissions.....	6
2.3.3 Mechanical Impedance Test.....	6
2.3.4 Radiographic Inspection.....	7
2.3.5 Computed Tomography Scan.....	7
2.3.6 Shearography.....	8
2.3.7 Vibrothermography.....	8
2.3.8 Infrared Thermography.....	9
2.4 Infrared Thermography Experimental Techniques.....	10
2.4.1 Optical Lockin Thermography.....	10
2.4.2 Pulse Thermography.....	11

2.5	Lockin Thermography Image Processing Techniques.....	13
2.5.1	Fourier Transform.....	13
2.5.2	Four-Point Method.....	13
2.5.3	Lockin Correlation.....	15
2.6	Infrared Imaging Systems .....	15
2.6.1	Photon Detectors.....	16
2.6.2	Thermal Detectors.....	16
2.7	Chapter Summary.....	17
3	Finite Element Modelling.....	18
3.1	Model .....	18
3.2	Material Properties .....	19
3.3	Initial Conditions.....	21
3.4	Thermal Flux Boundary Condition.....	21
3.5	Chapter Summary.....	22
4	Experimental Study .....	23
4.1	Experimental Layout.....	23
4.2	Infrared Camera .....	24
4.3	Samples .....	24
4.4	Excitation .....	25
4.5	Power Modulator.....	25
4.6	Function Generator.....	25
4.7	Chapter Summary.....	26
5	Data Analysis.....	27
5.1	Phase Contrast.....	27
5.2	Signal-to-Noise-Ratio .....	28
5.3	Surface Temperature Response.....	29
5.4	Image Processing .....	31
5.5	Camera Noise .....	32
5.5.1	Causes of Camera Errors .....	33
5.5.2	Simulation of Experimental Noise.....	34
5.6	Spatial Temperature Difference .....	35

5.7	Thermal Diffusion Length.....	36
5.8	Computed Tomography Scan.....	38
5.9	Chapter Summary.....	39
6	Influence of Excitation Frequency .....	40
6.1	Carbon Fibre Composite .....	40
6.1.1	Simulation Results .....	40
6.1.2	Experimental Results .....	43
6.2	Steel.....	46
6.2.1	Simulation Results .....	46
6.2.2	Experimental Results .....	48
6.3	Chapter Summary.....	49
7	Influence of Excitation Number of Wave Cycles.....	50
7.1	Carbon Fibre Composite .....	51
7.1.1	Simulation Results .....	51
7.1.2	Experimental Results .....	56
7.2	Steel.....	58
7.2.1	Simulation Results .....	58
7.2.2	Experimental Results .....	61
7.3	Chapter Summary.....	64
8	Influence of Excitation Power .....	65
8.1	Carbon Fibre Composite .....	65
8.1.1	Simulation Results .....	65
8.1.2	Experimental Results .....	68
8.2	Steel.....	70
8.2.1	Simulation Results .....	70
8.2.2	Experimental Results .....	73
8.3	Chapter Summary.....	74
9	Discussion, Conclusion and Recommendations.....	75
9.1	Discussion .....	75
9.2	Conclusion.....	77
9.3	Future Recommendations.....	78

References.....	79
Appendix A Sample Dimensions.....	84
A.1 Introduction.....	84
A.2 Carbon Fibre Sample Dimensions.....	84
A.3 Steel Sample Dimensions.....	86
Appendix B Infrared Basics.....	88
B.1 Infrared Radiation.....	88
B.2 Infrared Transmission Media.....	88
B.3 Infrared Thermography Approaches.....	89

## List of Figures

Figure 1: Surface temperature profile with time over defective and nondefective regions (from Sharath et al., 2013) .....	12
Figure 2: Four-point method image processing illustration (from Choi et al., 2008) .....	14
Figure 3: Lockin correlation image processing diagram (from Pitressi, 2015) .....	15
Figure 4: Finite element models showing the (a) front and (b) back surfaces.....	19
Figure 5: Heat capacity vs temperature plot for carbon/epoxy composite (from Kalogiannakis et al., 2004) .....	20
Figure 6: Through-thickness direction thermal conductivity vs temperature plot for carbon/epoxy composite (from Kalogiannakis et al., 2004).....	20
Figure 7: In-plane thermal conductivity vs temperature plot for carbon/epoxy composite (from Sweeting & Liu, 2004) .....	21
Figure 8: Marc Mentat model showing thermal flux boundary condition applied to front surface .....	22
Figure 9: Lockin thermography experimental setup.....	23
Figure 10: Phase difference between input and response signals (from Peng and Jones, 2010) .....	27
Figure 11: Areas considered as signal and noise for (a) Simulation and (b) experimental images .....	29
Figure 12: Typical surface temperature response and fitted curve representative of a d.c. component (Simulation data) .....	30
Figure 13: a.c. component of surface temperature response (Simulation data).....	30
Figure 14: Camera temperature measurement variation with time.....	32
Figure 15: Simulation phase images for CFRP at 0.2 Hz with noise peak-to-peak values of 0.05, 0.1, 0.2, 0.5 and 1°C .....	34
Figure 16: Simulation phase images for steel at 0.2 Hz with noise peak-to-peak values of 0.05, 0.1, 0.2, 0.5 and 1°C .....	34
Figure 17: Defect thermal contrast at varying depths for CFRP (Simulated data)	35
Figure 18: Defect thermal contrast at varying depths for steel (Simulated data) ..	36
Figure 19: CT scan results showing position of air bubble .....	38
Figure 20: CT scan results showing cross section dimensions of air bubble .....	39
Figure 21: Carbon fibre composite simulation phase images at 0.2, 0.1, 0.05, 0.02 and 0.01 Hz.....	41
Figure 22: Phase contrast plot for carbon fibre composite with 3000 W excitation .....	42
Figure 23: SNR for CFRP at varying defect depths vs frequency with 3000 W excitation intensity.....	43

Figure 24: Experimental phase image results for carbon fibre composite at 0.2, 0.1, 0.05, 0.02 and 0.01 Hz .....	44
Figure 25: Carbon fibre composite experimental phase contrast variation with excitation frequency.....	44
Figure 26: Carbon fibre composite SNR at varying defect depth.....	45
Figure 27: Steel simulation phase images at 0.2, 0.1, 0.05, 0.02 and 0.01 Hz .....	46
Figure 28: Phase contrast plot for steel at 3000 W .....	47
Figure 29: SNR for steel at varying defect depths vs frequency with 3000 W excitation intensity .....	48
Figure 30: Experimental phase image results for steel at 0.2, 0.1, 0.05, 0.02 and 0.01 Hz.....	49
Figure 31: Simulation data surface temperature results for CFRP at 0.1 Hz over defective and nondefective regions.....	50
Figure 32: Comparison CFRP simulation images obtained from using 5 (top) and 3 (bottom) cycles for defects at varying depths .....	52
Figure 33: Phase contrast plot for 3 and 5 cycles at 2 mm deep.....	53
Figure 34: Phase contrast plot for 3 and 5 cycles at 4 mm deep.....	53
Figure 35: Phase contrast plot for 3 and 5 cycles at 6 mm deep.....	54
Figure 36: SNR for steel at for 2 mm deep defect vs frequency for 3 and 5 wave cycles .....	55
Figure 37: SNR for steel at for 4 mm deep defect vs frequency for 3 and 5 wave cycles .....	55
Figure 38: SNR for steel at for 6 mm deep defect vs frequency for 3 and 5 wave cycles .....	56
Figure 39: CFRP phase image results after using 5 wave cycles against 3 at 0.2, 0.1, 0.05, 0.02 and 0.01 Hz .....	57
Figure 40: Phase contrast from using 3 against 5 excitation wave cycles.....	57
Figure 41: Experimental SNR plot for 2 mm deep defect .....	58
Figure 42: Comparison of steel simulation images obtained from using 5 (top) and 3 (bottom) waves cycles at varied defect depths and frequencies of 0.2, 0.1, 0.05, 0.02 and 0.01 Hz.....	59
Figure 43: Phase contrast plot for 3 and 5 cycles for 6 mm deep defect .....	60
Figure 44: SNR plot for 2 mm deep defect.....	61
Figure 45: SNR plot for 4 mm deep defect.....	61
Figure 46: Steel phase image results after using 5 wave cycles against 3 at 0.2, 0.1, 0.05, 0.02 and 0.01 Hz .....	62
Figure 47: Steel phase contrast comparison between experimental and simulation data with 5 excitation wave cycles .....	63
Figure 48: SNR comparison between simulation and experimental data.....	63
Figure 49: Carbon fibre composite phase images for 2 mm deep defect at 0.2, 0.1, 0.05, 0.02 and 0.01 Hz at varying excitation power intensities .....	66

Figure 50: Phase contrast plot for 10 mm diameter defect 2 mm from the surface .....	67
Figure 51: CFRP SNR of 2mm deep defect at 1500, 3000 and 6000 W .....	67
Figure 52: Experimental phase images for carbon fibre composite at 0.2, 0.1, 0.05, 0.02 and 0.01 Hz at varying intensities.....	68
Figure 53: CFRP phase contrast comparison at 1500, 3000 and 6000 W excitation power .....	69
Figure 54: Experimental CFRP SNR for 2 mm deep defect at 1500, 3000 and 6000 W.....	70
Figure 55: Steel phase images for 2 mm deep defect at 0.2, 0.1, 0.05, 0.02 and 0.01 Hz at varying excitation power intensities.....	71
Figure 56: Phase contrast trend for 2 mm deep defect at varying intensities .....	72
Figure 57: SNR for 2 mm deep defect at varying intensities.....	72
Figure 58: Experimental phase images for steel at 0.2, 0.1, 0.05, 0.02 and 0.01 Hz for varying intensities .....	73
Figure 59: Surface temperature response for steel at 0.2 Hz with 1500 W excitation intensity.....	74
Figure 60: Variation of phase contrast with frequency (from Ibarra-Castenado et al., 2004) .....	76
Figure 61: Carbon fibre sample dimensions and defect layout .....	84
Figure 62: Steel sample dimensions and defect layout.....	86
Figure 63: Infrared radiation on the electromagnetic spectrum (from Sultan et al., 2012) .....	88
Figure 64: Infrared transmission window .....	89

## List of Tables

Table 1: NDT techniques and detectable defects.....	9
Table 2: Magnitude of noise recorded over time.....	33
Table 3: Theoretically calculated thermal diffusion lengths for carbon fiber composite.....	37
Table 4: Theoretically calculated thermal diffusion lengths for steel .....	37
Table 5: Defect Dimensions and depth for carbon fibre sample .....	85
Table 6: Defect Dimensions and depth for steel sample .....	87

## Nomenclature

### Constants

$\pi$             3.1416

### Acronyms

<i>abs</i>	Absolute
CCD	Charge Coupled Device
CT	Computed Tomography
CFRP	Carbon Fibre Reinforced Polymer
FFT	Fast Fourier Transform
FPA	Focal Plane Array
GFRP	Glass Fibre Reinforced Polymer
HPC	High Performance Computer
<i>log</i>	Logarithm
LWIR	Long Wave Infrared
MCT	Mercury-Cadium-Telluride
NDT	Nondestructive Testing
NEDT	Noise Equivalent Temperature Difference
PMMA	Polymethyli-methacrylate
RMS	Root Mean Square
SNR	Signal-to-noise-ratio

## Variables

$A$	Amplitude	[ ]
$c$	Specific heat capacity	[J kg <sup>-1</sup> K <sup>-1</sup> ]
$e$	Thermal effusivity	[Ws <sup>1/2</sup> K <sup>-1</sup> m <sup>-2</sup> ]
$f$	Frequency	[Hz]
$F$	Harmonic force	[N]
$I$	Picture intensity	[ ]
$Im$	Imaginary values	[ ]
$k$	Thermal conductivity	[W m <sup>-1</sup> K <sup>-1</sup> ]
$N$	Noise	[ ]
$q$	Heat flux density	[W m <sup>-2</sup> ]
$Q$	Heat input	[W]
$Re$	Real values	[ ]
$S$	Signal	[ ]
$t$	Time	[s]
$T$	Temperature	[°C]
$T_0$	Initial change in temperature	[°C]
$v$	Velocity	[m s <sup>-1</sup> ]
$x$	Spatial coordinate	[ ]
$y$	Spatial coordinate	[ ]
$z$	Spatial coordinate	[ ]
$z$	Defect depth	[mm]
$Z$	Point impedance	[N s m <sup>-1</sup> ]

## Greek letters

$\Delta T$	Excess temperature	[°C]
$\Delta\varphi$	Phase difference	[Rad]
$\lambda$	Wavelength	[m]
$\mu$	Thermal diffusion length	[mm]
$\omega$	Angular frequency	[rad s <sup>-1</sup> ]
$\varphi$	Phase angle	[Rad]
$\rho$	Density	[kg/m <sup>3</sup> ]
$\sigma$	Standard deviation	[ ]

## Subscripts

<i>amb</i>	Ambient
<i>d</i>	Defective region
<i>max</i>	Maximum
<i>mean</i>	Mean
<i>min</i>	Minimum
<i>q<sub>o</sub></i>	Heat flux density
<i>range</i>	Variable range
<i>s</i>	Sound region
<i>sur</i>	Surface

# 1 Introduction

This study was focused on nondestructive testing (NDT) of carbon fibre reinforced polymers and mild steel using lockin infrared thermography. This was done with the aim of understanding how experimental and material parameters influence the ability to detect defects. The technique was only recently, in 2008, accepted as a standard NDT technique in the aerospace and other industries due to its unique advantages such as remote data acquisition, wide surface area inspection and faster inspection times. At Stellenbosch University, only in 2014 were studies developed aimed at promoting infrared thermography for nondestructive testing purposes. Kretzmann (2016) investigated pulse thermography for nondestructive testing of carbon and glass fibre composite laminates (CFRP & GFRP), polymethylmethacrylate (PMMA) polymer and industrial honeycomb samples. The study concluded that the type of flaw present in a sample affects defect contrast as thin defects are more challenging to detect than thick ones due to the low thermal resistance they create. Lamp and environmental reflections affected the ability to accurately reveal defects. To mitigate this, two lamps positioned on either side of the specimen were used. Maximum probable depth was not improved by heating duration time. In carbon fibre composite polymers defect visibility worsened. High heating power and longer excitation duration resulted in higher thermal contrast particularly in materials with low thermal diffusivity.

## 1.1 Background

Nondestructive testing comprises a variety of techniques used to evaluate the strength and integrity of materials without causing damage to them. There are numerous techniques in use today for testing different materials. A few of these techniques include ultrasonic testing, radiography, acoustic emissions, eddy current, visual inspection, computed tomography (CT) scans, shearography, and infrared thermography. All these techniques are valuable to production and expansion as they aid in reducing repair costs and equipment downtime, prevent catastrophes and extend the useful life equipment among other benefits.

Nondestructive testing techniques have a wide range of applications. Some of these include, but are not limited to, the determination of material properties such as density, elastic modulus, strength, surface hardness and absorption. Alternatively, they are used for corrosion and material flaw detection, strain measurements and reinforcement location (Servais, 2006). They can be applied to both new and

existing structures. In inspecting new structures, the techniques can be utilised for quality control in raw products such as forgings and castings while in secondary processed products they are used to check that the manufactured and finished components meet the expected standards for use. For old parts, NDT is used to check for new flaws and faults that a component might have developed in-service to ensure that it can still adequately perform its intended purpose.

Moela *et al.*, (2004) investigated the geometrical limitations in detecting defects in composite materials using infrared thermography. They used carbon and glass fibre composite materials with inclusions of varying sizes placed at different depths. It was noted that the thermal contrast was greater in the carbon fibre sample than in the glass fibre sample and this was attributed to the higher thermal conductivity of the carbon fibres and the increase in the relative conductivity between the basic material and the defects.

Moela *et al.*, (2013) investigated the capability of detecting slag inclusions and impact damage in carbon and glass fibre composites. They noted that inclusions as thin as 1/15 of their depth with thermal conductivity close to the material matrix could be detected. Furthermore, it was revealed that the technique was also effective in detecting impact damage resulting from low energy impact.

## 1.2 Motivation

Lockin thermography is an attractive nondestructive testing technique in that it is quick, fairly inexpensive to implement, equipment is readily available and is as effective as other established nondestructive testing techniques. It is non-contact and can be performed in-situ to inspect large areas at a time. Basic everyday components such as halogen lamps and phase angle controllers can be used for excitation and lamp modulation respectively while data acquisition via an infrared camera. Various studies in nondestructive testing have been conducted on a variety of materials with assorted defects aiming to establish lockin thermography performance charts. Studies on the influence of defect size, depth and thickness, influence of the excitation frequency, image processing and more all have illustrated the capability of defect detection using lockin thermography. Despite the expansion in knowledge that has been achieved, more is still to be done in understanding the interaction of various parameters. This research was aimed at understanding material and experimental parameters, excitation frequency, power and number of wave cycles, that promoted defect detection and an attempt was made to explain probable reasons for the results obtained.

## 1.3 Objectives

The main objectives of the study were to identify material and experimental parameters that enhanced defect detection in composite materials and as such carbon fibre was predominantly presented. Experimental parameter selections were biased towards lockin thermography nondestructive testing of carbon fibre composites and mild steel served as an alternative material of technique performance evaluation. The objectives were to:

- i. Model carbon fibre composite and mild steel specimen using finite element software to obtain a reference against which experimental results would be compared.
- ii. Investigate the influence of experimental parameters: frequency of thermal excitation, number of wave cycles and lamp intensity on the ability to reliably detect defects.
- iii. Investigate how accurate the proposed method is in detecting deep defects.
- iv. Investigate the influence of material properties on the ability to detect defects reliably.

## 1.4 Thesis Outline

The thesis is divided into nine chapters and two appendices. Chapter two being the literature review discusses the common flaws occurring in carbon fibre composites and the frequently used NDT techniques to detect them. It further discusses the two widely used infrared thermography experimental techniques, lockin thermography image processing techniques and types of infrared camera technologies. Chapters three and four are descriptions of finite element analysis simulations and experimental setups respectively. Chapter five discusses data analysis methods, experimental noise and CT scan results while chapters six, seven and eight discuss the effects lockin thermography parameters excitation frequency, number of wave cycles and intensity have on the ability to detect subsurface defects. In closing, chapter nine is summary of the findings with conclusions and recommendations.

## 2 Literature Review

This chapter is an overview of carbon fibre composite material flaws, nondestructive testing techniques, infrared thermography setups, image processing techniques and types of infrared detectors. The primary material in this study was carbon fibre composite as the method under study is widely used in the nondestructive testing of composite materials for flaws. To this end as prior stated, one of the objectives of this thesis was to investigate the extent to which material properties affected defect detection using lockin thermography for which steel was also included. The selection of steel was based on having dissimilar physical properties, higher thermal conductivity, heat capacity, density and is isotropic. As a result, steel was not thoroughly reviewed as it was merely a reference against which the carbon fibre composite material was contrasted.

### 2.1 Composite Defects

Fibre composite materials possess unique advantages due their high specific strength. They are able to withstand greater stresses than their individual constituents because of the fibre-matrix interaction which results in redistribution of the stresses (Schwartz, 2002). Despite this, they are prone to defects either during or immediately after manufacture or in-service. These defects may relate to the fibres, matrix, fibre-matrix bond, stacking or winding. In some instances, fibres may be folded or wavy rather than straight which results in a reduction in tensile and compressive strength or they may be hollow with extra-large diameter which may lead to stress concentrations and eventually premature failure. Defects arising from the matrix vary from failure to specify the correct resin for a particular application to using over-aged resins and contamination of the resin. Over-aging of the resin may be caused by storage at the wrong temperature or the time period that it was stored. Contamination relates to poor quality control processes during the manufacturing stage that may lead to impurities being introduced into the resin. Fibre-matrix debonding is another common defect that leads to premature component failure. The bond experiences shear forces when the component is under load. Weak bonds tend to break under the action of such forces which leads to the fibre separating from the resin, leaving discontinuities where failure originates. Stacking or winding defects arise from incorrectly oriented fibres. The fibres therefore carry loads that they were not designed for due to their positions in the matrix. Local misalignments of these fibres cause stress concentrations under load

which may lead to untimely failure of the material (Adams & Cawley, 1988; Servais, 2006).

## 2.2 Composite Damage

When a material is exposed to static, thermal, fluctuating and impact loads, it may fracture and composites are no exception. Under load, they may develop translaminar, interlaminar or transfibrous cracks. Translaminar cracks though not common lie perpendicular to the surface. Interlaminar cracks (delaminations) occur between the sheets and are the most common defect developed by composites in service. They arise mainly due to impact loads. Transfibrous cracks, also termed as fibre breakage, refer to the degradation of the fibres which leads to low strength of the material. This may arise due to water ingress or fiber-matrix debond (Cantell & Morton, 1992).

## 2.3 Nondestructive Testing Techniques for Composite Materials

With increasing demand for safety in engineering structures, nondestructive testing plays a vital role in ensuring that materials and parts used in these structures are free of defects. Most failure of components result from crack initiations at identifiable defects that grow and when large enough lead to failure. Therefore to prevent failure, these flaws ought to be detected and assessed in order to determine their impact on the load bearing capacity of a structure. When a material flaw degrades the performance of a component to levels where the component cannot satisfactorily perform its intended purpose it is termed a defect (Scott & Scala, 1982). Various nondestructive testing techniques are available to assess the integrity of components to ensure that they can perform according to their design specifications and a few are discussed.

### 2.3.1 Ultrasonic Testing

In ultrasonic nondestructive testing of composites, ultrasonic waves are directed into the material. When inside the waves are attenuated by viscoelastic effects,

inhomogeneity and defects. Ultrasonic nondestructive testing can reveal a wide variety of composite defects such as delaminations, porosities, contaminations and fibre orientations. These defects can be detected as they create a thin interface perpendicular to the ultrasonic wave path that obstruct its path. This is then captured by transducers and the data is further processed to reveal irregular wave transmission patterns. For a defect to be detectable using ultrasonic testing, it should lie parallel to the surface. Matrix cracks that lie parallel to the transmission path of the ultrasonic waves cannot be detected as they do not offer a wide enough reflecting surface except for significant levels of cracking where individual cracks join and create interlaminar delaminations (Steiner *et al.*, 1995; Aymerich & Meili, 1999).

### 2.3.2 Acoustic Emissions

Acoustic emission refers to the resulting stress waves produced when strain energy is released rapidly in a material due to microstructural changes. The principle behind this technique is to detect high frequency, low intensity stress waves produced by the specimen due to crack propagation and phase changes using a piezoelectric transducer. The amplified signal of the stress waves is then conditioned, recorded and analysed. The technique differs from other techniques in detecting fracture or deformation in that it utilizes information from the fracturing or deformation as they occur (Wevers, 1997). Unfortunately, this technique is hindered by the fact that composites, as opposed to isotropic materials, tend to attenuate and disperse the propagating stress waves and hence need a large number of sensors (Cantwell & Morton, 1992).

### 2.3.3 Mechanical Impedance Test

In this method, low-frequency mechanical waves are induced onto the surface of the material under test. The response is the point impedance,  $Z$ , which is calculated using Equation (2-1). The point impedance at a defect is lower than over sound areas of a specimen making it possible to detect the defects. The technique is more sensitive to defects that lie close to the surface of the specimen as the impedance change produced by a defect reduces as its depth increases. Using this technique, it is possible to detect voids and delaminations in laminated structures but is insensitive to translaminar cracks (Cawley, 1984).

$$Z = \frac{F}{v} \quad (2-1)$$

$F$  is the harmonic force input to the structure and  $v$  is the resultant velocity of sound in the structure at the same point.

### 2.3.4 Radiographic Inspection

Radiographic inspection of composites is based on the absorption and penetration of x-rays or gamma rays. As these pass through a material, they are differentially absorbed in areas of varying densities which include excess material (inclusions) or missing material (voids and porosity). Therefore radiographic inspections are based on the variation of density within the material to detect and locate defects, the greater the thickness, the greater the absorption. The rays are then captured on a photographic film to produce an image. Voids in a material show up as darkened areas due to more radiation reaching the film on a clear background (Willcox & Downes, 2003). For composites, x-ray radiography is difficult because the absorption characteristics of the fibres and the matrix are similar and the overall absorption of the material is very low. It is difficult to detect delaminations as they lie normal to the radiation therefore contribute little to the overall absorption while voids and translaminar cracks can be detected if they are of appreciable size compared to the sample thickness (Adams & Cawley, 1988).

### 2.3.5 Computed Tomography Scan

Computed tomography scans apply x-rays to probe a test object to produce two and three dimensional images of objects from the x-ray images. This is a variation to the conventional x-ray radiography in that image processing involves reconstruction of the two dimensional images to obtain three dimensional images (Gao & Kim, 1999). The system comprises a radiation source, imaging system and a turntable stage located in between these two components. In order to represent the object accurately, the turntable and the imaging systems are connected to a computer that, with specialised software, correlates the position of the object with the resulting image and produces three dimensional images. The resulting images from the scan can contain information about the internal and external structure of

the object such as dimensions, density, shape and internal flaws (Krumm *et al.*, 2012).

### 2.3.6 Shearography

This is an interferometric method which employs laser light and an image shearing camera to identify defects in a specimen. When the test surface is illuminated with the laser light, the image shearing camera captures the surface reflected light and produces two sheared images in the image plane. The two images interfere with each other and produce a speckle pattern. Since defects in a material induce strain concentrations, shearography nondestructive testing reveals defects by identifying the defect-induced strain concentrations. Testing is done on the specimen before and after loading and the two speckle images are superimposed producing a fringe pattern which depicts the surface strain distribution. An anomaly in the fringe pattern indicates defect-induced strain concentrations and the severity of which can be determined by the degree of strain concentrations. Despite measuring the surface strain distribution, shearography nondestructive testing has the ability to detect both surface and internal flaws as the latter also influence surface deformation unless they are located very remotely from the test surface. Delaminations in composites can effectively be identified using this method. Broken fibres, matrix cracking and moisture presence can also be identified but the analysis of the fringe anomalies is not straightforward (Hung, 1996).

### 2.3.7 Vibrothermography

This method, sometimes called ultrasound thermography or thermosonics, employs mechanical waves to directly excite the internal defects without the need of heating the surface of the material. Unlike electromagnetic waves, mechanical waves cannot travel through a vacuum and thus need a medium to travel through. They travel faster in solids and liquids than through air therefore vibrothermography requires a coupling between the transducer and the specimen to reduce losses. Common coupling media are water, water-based gels, fabrics or aluminium. Once in the material, the ultrasonic waves travel freely if the material is homogenous. If the material is defective, the waves will be absorbed, scattered, spread or dispersed when they come across a heterogeneity. This results in heat generation at the defect which is observed via an infrared detector system. The technique is ideal for defect detection as it is independent of the orientation of the defect inside the specimen

enabling detection of both internal and open surface defects. It is effective in the detection of cracks and delaminations (Ibarra-Castanedo *et al.*, 2009).

### 2.3.8 Infrared Thermography

In this technique, infrared energy is introduced onto the surface of a sample and the resulting temperature variation is captured remotely using an infrared camera. The heat flows uniformly through the sample until it reaches a heterogeneity where it gets reflected and spreads out. Defective regions are detected due to their discrete thermal and physical properties compared with nondefective regions which include density, thermal conductivity and heat capacity (Avdelidis *et al.*, 2004). Defects that can be detected with this method include delaminations, water ingress, inclusions and impact damage. Table 1 is a summary of the nondestructive testing techniques discussed and their detectable defects.

Table 1: NDT techniques and detectable defects

<b>NDT Technique</b>	<b>Detectable Defects</b>
Ultrasonic testing	Delaminations, porosities, inclusions, and fibre orientations
Acoustic emissions	Delaminations and impact damage
Mechanical impedance	Voids and delaminations
Radiographic inspection	Inclusions, voids, translaminar cracks and porosity
CT scan	Delaminations, cracks, voids, inclusions and fibre orientation
Shearography	Delamination broken fibres, cracks and moisture presence
Vibrothermography	Cracks and delaminations
Infrared Thermography	Impact damage, delaminations, inclusions and water ingress

## 2.4 Infrared Thermography Experimental Techniques

Infrared thermography can be classified according to how the excitation is applied namely pulse and lockin thermography. The two are distinctively different but are used in the inspection of similar components and structures. Further, image processing techniques of the resultant temperature fields differ. Despite the two techniques being employed in similar applications, lockin thermography defect depth probing capabilities are much higher than pulse thermography hence deeper defects can be detected (Chatterjee *et al.*, 2011).

### 2.4.1 Optical Lockin Thermography

Periodically modulated heat waves are deposited onto the surface of a sample which then propagate inwards and get reflected back to the surface when they encounter heterogeneous material (Bates *et al.*, 2000). The reflected wave then interferes with the oncoming wave and produces an interference. From the resulting wave, the amplitude and phase are measured and processed to obtain amplitude and phase images. In the phase images, local colour variations represent a variation in phase angle which signifies local variation of material properties. The resultant surface temperature as a function of time and distance from the surface based on a one-dimensional heat transfer model is given by Equation (2-2) (Moela *et al.*, 2013; Zimnoch *et al.*, 2010).

$$T(x, t) = T_0 e^{-\frac{z}{\mu}} \cos\left(\frac{2\pi z}{\lambda} - \omega t\right) = T_0 e^{-\frac{z}{\mu}} \cos\left(\omega t - \frac{2\pi z}{\lambda}\right) \quad (2-2)$$

where the initial change in temperature produced by the wave is given by  $T_0$ , defect depth by  $z$ , thermal diffusion length by  $\mu$  while the angular frequency  $\omega = 2\pi f$  and the thermal wavelength  $\lambda = 2\pi\mu$ . The thermal diffusion length is the depth at which the intensity of the thermal wave drops to  $1/e$  of that at the surface of the sample. It signifies the depth at which a defect will be detectable for a particular frequency of excitation used. This is dependent on the excitation frequency and thermal properties of the material (thermal conductivity  $k$ , specific heat capacity  $c$  and density  $\rho$ ). From Fourier's law, the solution to the one dimensional heat transfer equation for periodic thermal waves propagating through a semi-infinite homogenous material, the thermal diffusion length is given by Equation (2-3).

$$\mu = \sqrt{\frac{k}{\pi f \rho c}} \quad (2-3)$$

From the above equation, the thermal diffusion length is inversely proportional to the excitation frequency. A high modulation of heat flux frequency restricts the excitation thermal wave to the surface of the specimen while a low modulation frequency allows for the heat wave to penetrate deeper into the specimen. In order to probe deep defects, the excitation frequency is chosen correctly so as to allow adequate diffusion of the heat wave into the specimen.

This technique is advantageous when compared with other optical thermography techniques as it is insensitive to non-uniform heating and surface emissivity variations. But despite this, a major drawback is the presence of local noise which is high when the thermal amplitude is low which in turn affects the phase of the response (Moela & Carlomango, 2004). Another setback is the presence of blind frequencies which are frequencies at which a defect does not show a phase shift in spite of its depth being below the thermal diffusion length. This is caused by three dimensional heat transfer effects (Chatterjee *et al.*, 2013). It is worth mentioning that as the frequency of the excitation is lowered, phase contrast values of a defect change signs at blind frequencies. For industrial applications these frequencies should be avoided as they possess risks of passing defective material based on the failure to detect a defect. For academic purposes, these frequencies are important as they can aid in the estimation of defect depth or the extension in depth of the defective region.

The phase response to the excitation varies depending on the defect size, larger defects exhibit higher phase values than smaller ones at the same depth. Additionally, because of this lower phase contrast shown by smaller defects, three dimensional heat flow decreases the probability of detection of small defects more than large defects (Ghali *et al.*, 2011).

#### 2.4.2 Pulse Thermography

In this method, the surface is instantaneously heated by means of high power lamps which can be xenon flash lamps or halogen lamps to mention a few. The duration of the pulse varies from milliseconds to several seconds depending on the power of the lamps, the materials being inspected and the depth of the defects. After the pulse is introduced onto the sample surface, the thermal energy rapidly diffuses into the

material which results in a disparity in surface temperature distribution depending on the rate of diffusion at different places on the sample. An example of such a disparity in temperature between defective and nondefective places would be as shown in Figure 1.

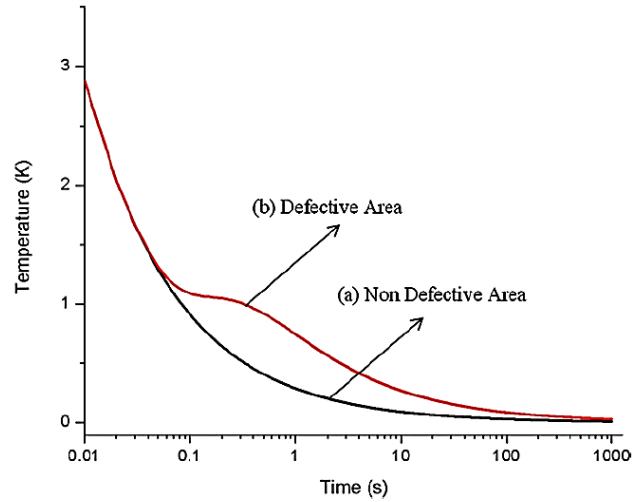


Figure 1: Surface temperature profile with time over defective and nondefective regions (from Sharath *et al.*, 2013)

Surface artefacts, emissivity variation and non-uniform heating greatly affect interpretation of results in this technique as opposed to lockin thermography. Their influence on the surface temperature distribution is significant and can lead to misinterpretation of results. The surface temperature with respect to time is given by Equation (2-4).

$$T_{sur}(t) = \frac{Q}{e\sqrt{\pi t}} \quad (2-4)$$

$$e = \sqrt{k\rho c} \quad (2-5)$$

where  $Q$  is the input energy,  $t$  is the time and  $e$  is the thermal effusivity which is a measure of how fast a material changes temperature. Therefore if the material has a variation in effusivity, the surface temperature will vary. Materials with low effusivity values show higher temperature rises hence defect detection is enhanced (Ibarra-Castanado *et al*, 2013).

## 2.5 Lockin Thermography Image Processing Techniques

Contrary to pulse thermography for which a great variety of image processing techniques are available, only a few signal processing techniques are commonly used for lockin thermography data. These are based on the extraction of phase and amplitude information of the surface temperature response. Phase images in particular offer significant advantages over amplitude images as they are less affected by environmental reflections, emissivity variations, non-uniform heating, surface orientation and geometry than amplitude images hence are mostly used for image analysis (Ibarra-Castenido *et al*, 2004).

### 2.5.1 Fourier Transform

The fast Fourier transform (FFT) is applied to the temperature profile of each pixel. From the resulting Fourier spectrum, the amplitude and phase at the lockin frequency can be extracted. It is from these amplitude and phase values that the amplitude and phase images are constructed respectively. Using the FFT for lockin thermography data analysis is advantageous as its application is not restricted only to sinusoidal excitation modulation but can also be used on square waveforms (Duan *et al.*, 2013) The FFT is calculated from Equation (2-6).

$$F_n = \sum_{k=0}^{N-1} T(k)e^{\frac{2\pi i k n}{N}} = Re_n + iIm_n \quad (2-6)$$

where  $T(k)$  = surface temperature at a location in the  $k$ th image,  $Re_n$  = real part,  $iIm_n$  = imaginary part,  $N$  = frequency increment. From the FFT results, the phase and amplitude responses are calculated from the real and imaginary parts of the Fourier spectrum by Equation (2-7) respectively.

$$\varphi_n = \tan^{-1}\left(\frac{Im_n}{Re_n}\right) \quad A_n = \sqrt{Re_n^2 + Im_n^2} \quad (2-7)$$

### 2.5.2 Four-Point Method

This method involves obtaining four equidistant data points within a wave cycle. From these points, the amplitude and phase of the wave can be extracted to derive

the amplitude and phase images respectively. This is the most widely used technique but its effectiveness highly depends on the excitation being strictly sinusoidal and the response signal having low noise. These reduce defect detection capabilities when using phase images as they lead to false results (Pitaressi, 2012). To improve this, more points may be chosen per wave and averaged rather than one set, experimental data may be curve fitted or the number of wave cycles can be increased (Krapez *et al.*, 1998). Figure 2 shows the positions of the points selected for manipulation relative to the excitation wave and their labels. From the points, the amplitude and phase images are worked out from Equations (2-8) and (2-9) respectively.

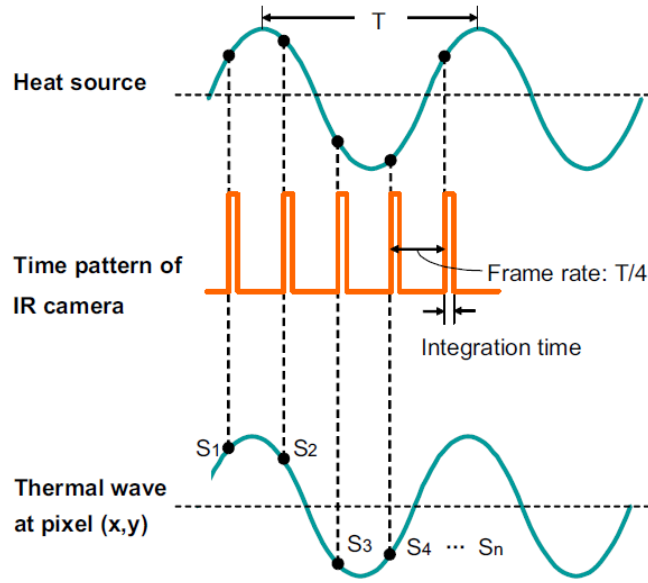


Figure 2: Four-point method image processing illustration (from Choi *et al.*, 2008)

$$A(x, y) = \sqrt{(S_1(x, y) - S_3(x, y))^2 - (S_2(x, y) - S_4(x, y))^2} \quad (2-8)$$

$$\varphi(x, y) = \tan^{-1} \left[ \frac{S_1(x, y) - S_3(x, y)}{S_2(x, y) - S_4(x, y)} \right] \quad (2-9)$$

### 2.5.3 Lockin Correlation

This technique comprises the sin/cos correlation which simulates the principle of a two channel lockin amplifier. Phase and amplitude information can be extracted at a variety of frequencies of interest from signals buried in statistical noise. In order to accomplish this, a reference signal at the exact frequency as the excitation, lockin frequency, is correlated with the surface temperature response and relevant data is obtained. It also acts as a narrow band filter which increases the defect to noise ratio (Pitressi, 2015). To avoid erroneous results, the processed temperature signal should only be the a.c. component and the applied thermal excitation must be periodically amplitude modulated (Breitenstein *et al.*, 2010). Figure 3 is an illustration of the lockin correlation principle showing data manipulation processes.

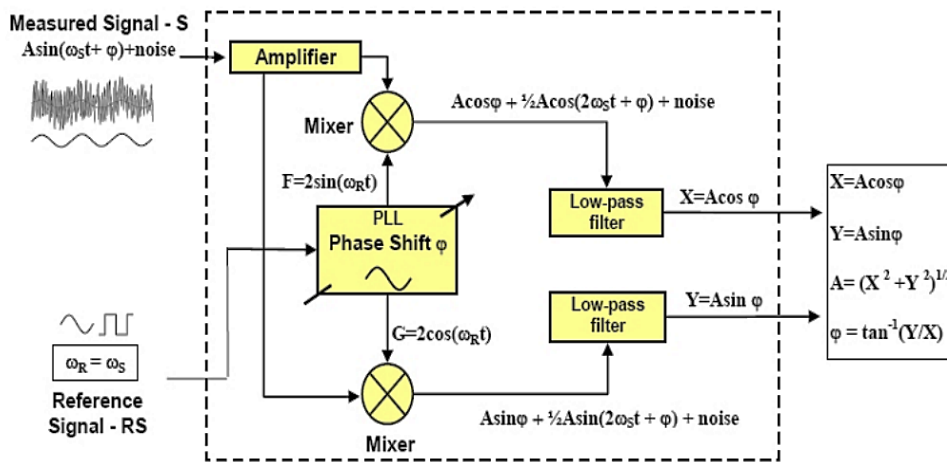


Figure 3: Lockin correlation image processing diagram (from Pitressi, 2015)

## 2.6 Infrared Imaging Systems

Early infrared cameras had a single infrared detector that recorded scene temperatures serially from point-to-point to capture the whole scene (Griffith *et al.*, 2002). They used quantum detectors (photodiode type) usually cooled with liquid nitrogen that were manufactured from a variety of detector materials such as indium-antimonide (InSb) and mercury-cadmium-telluride (MCT, HgCdTe). The two detector types are sensitive in distinct wave bands. InSb is sensitive in the mid-range spectrum (3 - 5  $\mu\text{m}$ ) whereas MCT sensitivity ranges from the mid-range to the long wave region (8 - 10  $\mu\text{m}$ ).

Modern infrared cameras use multiple detectors in an array to record scenes of temperature and are termed focal plane array (FPA) cameras. Similar to silicon-based CCD cameras working in the visible range, FPAs employ two-dimensional arrays of detectors within the focal plane of the infrared optics. Also, just as the early cameras, they can be manufactured from either InSb or MCT to capture infrared radiation in the wave bands aforementioned. To obtain the image, each photodiode of the array is electrically connected to a readout channel of a separate silicon readout-chip which is attached to the detector chip.

Based on the atomic interactions, these detectors are classified either as intrinsic or extrinsic. Intrinsic detectors are based on the excitation of electrons from the valence band to the conduction band while extrinsic detectors excite electrons into the conduction band or holes to the valence band from impurity states within the band. To achieve higher sensitivity, extrinsic detectors have to be cooled as opposed to intrinsic detectors which are uncooled. Therefore, in uncooled systems thermal and optical transitions rise and tend to compete which increases noise in captured images (Rogalski. A, 2012).

### 2.6.1 Photon Detectors

Sometimes called quantum detectors, when an incident photon strikes the detector it stimulates a free charge that is collected and amplified by an electronic circuit. The charge produced is due to a change in the electronic energy distribution of the detector material. These detectors are wavelength dependant for highest signal-to-noise-ratio and sensitivity per unit incident radiation power. Notable to these detectors is the cryogenic cooling that inhibits the generation of charge carriers reducing noise in the captured images (Griffith *et al.*, 2002).

### 2.6.2 Thermal Detectors

Thermal radiation incident on this type of detector is absorbed by the detector material which is made out of a passive energy absorbing material. This then causes an increase in detector temperature proportional to its radiosity. The temperature is then determined by scaling a temperature dependent property such as electrical conductivity. Thermal effects induced in the detector are dependent on radiant power of the radiation and are independent of wavelength and the spectral content (Rogalski. A, 2003). For performance enhancement, these detectors are isolated

from the environment and substrate. Compared with photon detectors, they have slower response times and are less sensitive. Detector sensitivity is expressed by the noise equivalent temperature difference (NEDT) which is the change of incident radiation that gives an output signal equal to the RMS noise level. This is proportional to the square of the thermal conductance while the detector response time is inversely proportional to the thermal conductivity. Therefore camera performance is a trade-off between sensitivity and response time.

## 2.7 Chapter Summary

This chapter highlighted common flaws found in fibre composite materials as well as techniques used to detect them. The flaws included matrix cracks, interlaminar and translaminar cracks, fibre breakage, fibre-matrix bond failure to mention a few. Nondestructive testing techniques covered were ultrasonic, acoustic emissions, mechanical impedance, conventional radiography, CT scans, shearography, vibrothermography and infrared thermography. Infrared thermography nondestructive testing experimental setups of lockin and pulse thermography as well as lockin thermography image processing techniques were reviewed. And finally the chapter concluded with a review of infrared imaging systems and detectors.

### 3 Finite Element Modelling

This chapter discusses the finite element analysis that was performed to simulate lockin thermography. The purpose of this was to understand how the technique performs under ideal conditions of consistent material properties, no interaction with other defects and no environmental noise in order to predict the possible outcome of experimental results. The models used were sections of the sample representing the 10 mm wide defect at depths of 2, 4 and 6 mm from the surface. The defect type simulated was a flat bottom hole as it was reasonably easy to physically fabricate. The analysis was conducted using Marc Mentat 2015 software.

#### 3.1 Model

The model dimensions were blocks of  $50 \times 50 \times 8$  mm. The size of the defect was 10 mm wide. This size was selected to study how small defects responded to the technique and the extent defect depth affected their detectability. Bigger defects were more easily detectable. Brick elements were used in all the samples, which resulted in a uniform mesh. The models had anywhere between 78,560 and 79,896 elements and nodes from 84849 to 85801. Transient thermal analysis was conducted and the temperature histories of the nodes of interest over the duration of the excitation were obtained for post-processing. Due to the numerous parameters, excitation frequency, power, number of wave cycles and material, that were investigated and the numerous models developed, Stellenbosch University's high performance computer (HPC) was used to solve the models as it provided more computational power which significantly reduced simulation times. The same models were used for both carbon fibre and steel, the only difference being the material properties assigned to each. For carbon fibre, different values of the thermal conductivity were assigned for the through thickness and in-plane directions due to its orthotropic nature. For mild steel, the properties were constant in all directions it being isotropic. The values used were adapted from Sweeting & Lui (2004), Kalogiannakis *et al* (2004), Joven *et al* (2012) and matweb.com. Figure 4 (a) and (b) are illustrations of the models showing the front face where the excitation was applied and the rear respectively.

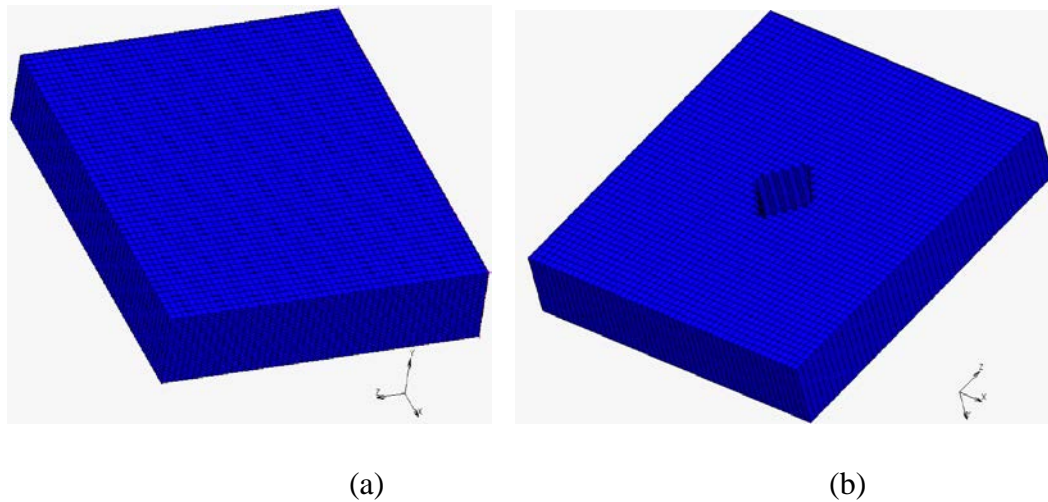


Figure 4: Finite element models showing the (a) front and (b) back surfaces

## 3.2 Material Properties

Composite thermal properties, heat diffusion and specific heat, present a high variation with respect to temperature. This dependence is linear. The composite matrix has three characteristic stages namely the preglass, glass and postglass transition stages. The transition significantly affects the thermal conductivity and the heat capacity. Further, composite material properties depend strongly on material composition, fibre-to-resin ratio and fibre orientation.

The gradient of the heat capacity curve increases during the glass transition stage and then decreases to a gradient lower than during preglass transition stage once the transition stage is complete. Figure 5 is an illustration of the variation of the heat capacity with temperature for carbon fibre epoxy composite over the range -30 to 170 °C.

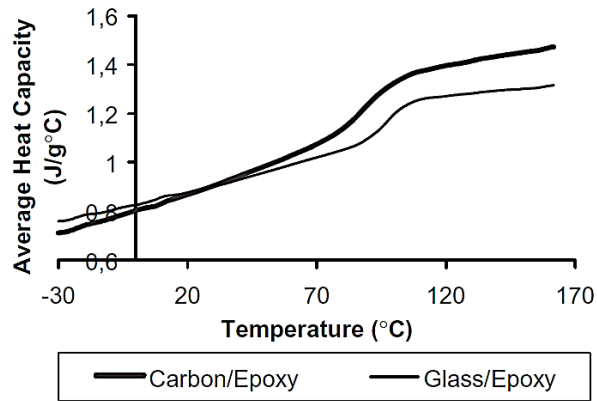


Figure 5: Heat capacity vs temperature plot for carbon/epoxy composite (from Kalogiannakis *et al.*, 2004)

For the thermal conductivity, it decreases during the glass transition stage reaching a minimum at the end of the stage and then raises to a gradient higher than the pre-glass stage over the temperature range of interest of 10 to 110 °C. This is illustrated in Figure 6. In the case of the in-plane thermal conductivity, the values were higher than in the through-thickness direction by a factor of approximately four. This is depicted in Figure 7. For steel, the properties were fairly consistent for the temperature range of the simulations as the overall temperature rise was low. The thermal conductivity used was 51.9 W/m K, the heat capacity was 472 J/g °C and the density was 7858 kg/m<sup>3</sup> (matweb.com).

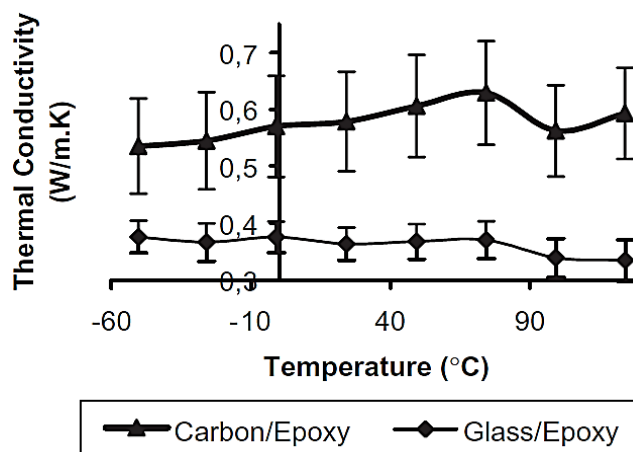


Figure 6: Through-thickness direction thermal conductivity vs temperature plot for carbon/epoxy composite (from Kalogiannakis *et al.*, 2004)

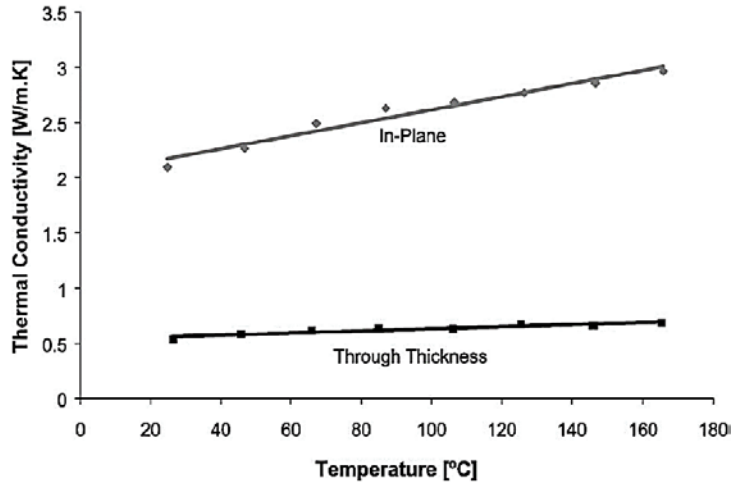


Figure 7: In-plane thermal conductivity vs temperature plot for carbon/epoxy composite (from Sweeting & Liu, 2004)

### 3.3 Initial Conditions

Ambient room temperature was set as the initial temperature in all the models. It represents a uniform temperature distribution throughout the sample as it was assumed to be in thermal equilibrium. In all models, the influence of convection and radiative heat transfers were neglected due to prior simulations that showed high similarity between phase image results obtained from applying or neglecting the heat transfer mode. Other authors in literature such as Ranjit *et al*, (2015) obtained accepted results from simulations conducted with the neglect of radiative and convective heat transfers. The temperature initial condition is as shown in Equation (3-1).

$$T(x, y, z, t = 0) = T_{amb} = 25^{\circ}C \quad (3-1)$$

### 3.4 Thermal Flux Boundary Condition

A sinusoidal thermal flux was applied to the front surface of the model. The surface had 2500 elements and 2601 nodes. The radiation applied was perpendicular to the element surfaces. An emissivity of 0.92 was assigned to all faces on the top elements to ensure a high absorption of the applied radiation and to attain uniform high emissivity. This was done in order to match experimental samples where the

surfaces were painted black, the reason for this is explained in the next chapter. A Marc Mentat model depicting the application of the flux is shown in Figure 8.

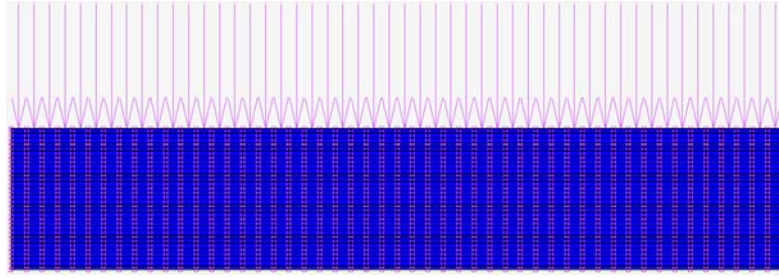


Figure 8: Marc Mentat model showing thermal flux boundary condition applied to front surface

This boundary condition in Marc Mentat was achieved with the aid of the tables function. The heat flux had two components, an alternating temperature part (a.c.) and a constant temperature rise part (d.c). The  $\frac{q_{max}}{2}$  part was the component that resulted in a constant temperature rise while the  $\frac{q_{max}}{2} (\cos(2\pi ft))$  component resulted in sinusoidal temperature variations with peak-to-peak amplitude of  $\frac{q_{max}}{2}$ . The equation that represents the thermal wave is given by Equation (3-2).

$$q_o = \frac{q_{max}}{2}(1 + \cos(2\pi ft)) \quad (3-2)$$

where  $q_o$  is the heat flux density,  $q_{max}$  is the maximum heat flux density,  $f$  is the frequency of the thermal excitation.

### 3.5 Chapter Summary

A transient three dimensional thermal analysis was performed on the models in order to account for lateral heat diffusion. The results from simulations, which were the surface nodes temperature evolution with time, were then further processed in order to extract phase information about the response. The initial and boundary conditions were an initial temperature of 25°C that was representative of room temperature and a thermal flux applied on the surface of the sample of varying frequency, intensity and wave cycles.

## 4 Experimental Study

An account of the layout is presented showing the equipment and test sample relative positions. The equipment used were an infrared camera, plain weave carbon fibre composite, mild steel, halogen lamps, function generator and power module. An oscilloscope was used for reference signal amplitude adjustment as the power output of the lamps was proportional to the reference signal's peak-to-peak value. The function generator used had analogue controls and as such the frequencies used were best approximations. Camera specifications are laid out including carbon fibre composite preparation.

### 4.1 Experimental Layout

The setup consisted of  $2 \times 1500\text{ W}$  and  $4 \times 1000\text{ W}$  halogen lamps, tripod stand, phase angle controller, FLIR E60 infrared camera, function generator and laptop computer. The function generator provided the reference signal used for lamp modulation. To set the period, a stop watch was used as the function generator used as aforementioned had analogue dials. This signal from the function generator was fed to the phase angle controller which modulated the lamp intensity with respect to the signal. The data was then captured using the FLIR E60 infrared camera and the videos processed using MATLAB<sup>TM</sup> software. It should be noted that the excitation and the camera were not synchronised automatically as the camera did not have remote triggering functions therefore the triggering was done manually for both the lamps and the camera. The experimental setup is shown in Figure 9.

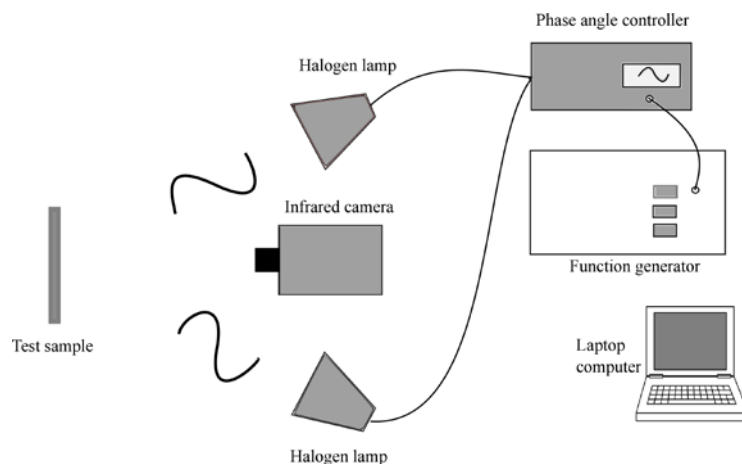


Figure 9: Lockin thermography experimental setup

## 4.2 Infrared Camera

The experiments were conducted with a FLIR E60 infrared camera with thermal and spatial resolutions of 0.05 °C at 30 °C and 240 × 320 pixels respectively. The camera employs a focal plane detector array with uncooled microbolometer detectors that operate in the long wavelength infrared (LWIR) region between 7.5 – 13 μm. It had a maximum frame rate of 30 Hz and a temperature measurement range of – 20 °C to 650 °C. This type of camera for infrared lockin thermography is mostly used where high defect sensitivity is not required. Modern infrared thermography cameras based on quantum detectors with high sensitivity, frame rate and resolution are cooled with liquid nitrogen using Stirling coolers to below 80 K. This difference in detector operating temperature and sensitivity makes cooled detectors more accurate than uncooled ones by factors of between 2 - 4 (Breinstein *et al.*, 2010).

## 4.3 Samples

The materials used were mild steel and carbon fibre composites. In both cases the samples had dimensions of 180 × 180 × 8 mm with flat bottom holes drilled on a wide face. For steel, the holes could be drilled on either of the two wide faces but for the carbon fibre sample, they were drilled on the surface away from the one that made contact with the tool during cure. All samples were painted black on the excitation receiving surface to increase radiation absorption and attain uniform emissivity cross the surface. As one would recall, boundary conditions similar to these were prescribed in the simulations where an emissivity of 0.92 was assigned to the surface of the models. The sample diagrams and dimensions are shown in Appendix A.

The carbon fibre composite sample was made from plain-weaved prepreg laminates. The parent material was cut into square pieces of 180 × 180 mm and stacked together. A total of 32 laminates were used to produce a sample thickness of 8 mm. The sample was then vacuum bagged and placed in an oven for 2 hours at 120 °C to cure. During cure, excess resin was soaked up by a piece of foam placed over the sample. Before laminate layup, a release agent was smeared on the curing tool to prevent the curing sample from sticking to it. Prepregs were chosen for this study due to their more uniform density distribution, shorter curing time, less excess resin, are not too demanding to layup and have high probability of obtaining a multiple of finished parts with high similarity when compared with manual composite layup.

## 4.4 Excitation

Tungsten halogen lamps were used to excite the samples. They were placed on either side of the test sample to accomplish matched heating. To achieve maximum direct heating, lessen optical reflections and get the most heat from the lamps, the glass covers over the lamps were removed as they tended to heat up during experiments adding a heat component phenomena that was not accounted for in the finite element simulations.

## 4.5 Power Modulator

A united automation FC11AL/2 universal phase angle controller was used to interface the function generator and the lamps. Its purpose was to modulate the intensity of the lamps with respect to the reference signal from the function generator. In order to modulate the power of the excitation as earlier pointed out in the chapter introduction, the amplitude of the reference wave was appropriately adjusted as the power output of the lamps was proportional to the reference wave signal peak-to-peak value. It had a low voltage operating input signal range of 1.5 to 5 VAC corresponding to minimum and maximum lamp intensity respectively. And as such lay the minimum and maximum voltage range of the input signal from the function generator. The combined power of the halogen lamps was 7000 W and depending on the maximum lamp peak power required, a fraction of the maximum reference voltage signal was set which corresponded to the lamp power required. Also, being a solid-state piece of apparatus, the module was mounted onto a heat sink for cooling.

## 4.6 Function Generator

A Goldstar FG 8002 function generator was used to provide the sinusoidal signal to the phase angle controller. This signal was used as the reference for lamp modulation. Various frequencies and amplitudes were set to vary the lamp response. This apparatus as prior mentioned had analogue knobs for frequency, amplitude and offset setting. The minimum frequency permissible was 0.008 Hz which corresponded to a wave cycle time of 120 seconds. In order to account for the phase angle controller operating voltage range, 1.5 - 5 VAC, the reference signal from the function generator was offset upwards in order to evade negatives and values below 1.5 VAC.

## 4.7 Chapter Summary

This chapter was a brief discussion of equipment that were used for experimental study. Lockin infrared thermography is a fairly inexpensive technique with regards to experimental setup. The setup in the present scenario was comprised a FLIR E60 infrared camera operating in the medium to long infrared wavelength band with uncooled microbolometer detector elements. The carbon fibre composite sample consisting of prepreg laminates was oven cured at 120 °C for two hours while the mild steel was industry supplied. A set of  $2 \times 1500$  W and  $4 \times 1000$  W lamps were used and lamp intensity modulation was achieved by adjusting the reference signal voltage peak-to-peak value. This was done with the aid of an oscilloscope. To modulate the excitation intensity, a universal phase angle controller was used that modulated the lamp intensities with respect to the reference signal from the function generator.

## 5 Data Analysis

This chapter discusses the analyses that were performed on simulation and experimental data. They included phase contrast and signal-to-noise-ratio (SNR) measurements as indicators of determining the probability of defect detection. Also, definitions of the phase contrast and signal-to-noise-ratio are presented. Thereafter discussions on image processing procedures, effect of noise, CT scan results and theoretical calculations on detectable defects are presented.

### 5.1 Phase Contrast

Lockin thermography analysis is based upon the detection and analysis of the thermal wave response of a sample to an excitation. To this end, of interest are the phase and amplitude. The phase information can be used to estimate the depth of a defect and physical properties of materials (Peng and Jones, 2013) while the amplitude image can be used to determine the defect dimensions (Ranjit *et al.*, 2015). In lockin thermography, a defect is defined as the phase difference between the sound and defective regions (Choi *et al.*, 2008). Therefore for a defect to be detected, the thermal response of the defective area should have a distinct contrast to the sound area. It should be noted however that both the sound and defective areas exhibit a phase shift with reference to the reference signal but their magnitudes differ. Figure 10 is an illustration of this showing a typical phase shift of the response signal compared to the input signal.

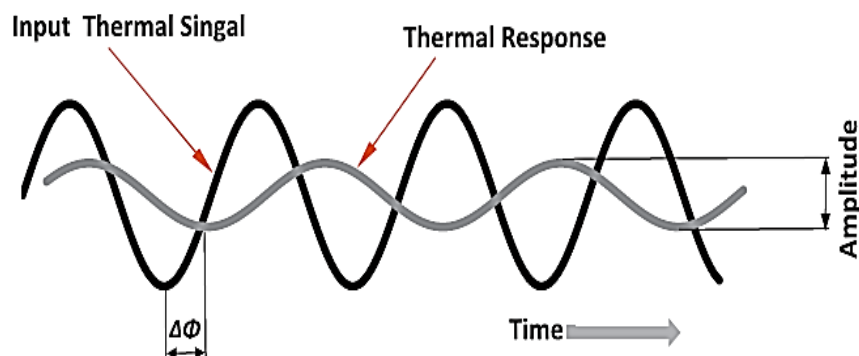


Figure 10: Phase difference between input and response signals (from Peng and Jones, 2010)

The phase is not only less sensitive to non-uniform heating and emissivity variations but also to environmental reflections. When compared with amplitude images, it provides deeper probing capabilities (Junyan *et al.*, 2013; Susa *et al.* 2006). Despite the numerous advantages, phase images are susceptible to noise interference which is high when the response thermal amplitude is low (Moela *et al.*, 2013). Thus for a defect to be detectable, the phase contrast between defective and nondefective areas has to be greater than the detector noise (Wallbrink *et al.*, 2007). Equation (5-1) defines the phase contrast.

$$\Delta\varphi(x, y) = \varphi_d(x, y) - \varphi_s(x, y) \quad (5-1)$$

where  $\varphi_d(x, y)$  is the phase value at pixel  $(x, y)$  over a defective area and  $\varphi_s(x, y)$  is the phase value at pixel  $(x, y)$  over a sound region.

In order to increase the contrast between the defects and the sound material, the images were normalized. The normalized phase image was defined by Equation (5-2).

$$\Delta\varphi(x, y) = \frac{\Delta\varphi_{max} - \Delta\varphi(x, y)}{\Delta\varphi_{max} - \Delta\varphi_{min}} \quad (5-2)$$

where  $\Delta\varphi_{max}$  is the maximum phase contrast value in the image,  $\Delta\varphi(x, y)$  is the phase contrast value of the pixel of interest and  $\Delta\varphi_{min}$  is the minimum phase contrast value in the image.

## 5.2 Signal-to-Noise-Ratio

The probability of defect detection using lockin thermography is dependent on attaining a significant thermal contrast between the defect and the sound material (Lahiri *et al.*, 2012). To this effect, defects that exhibit a low contrast have a high probability of going by undetected. Therefore, in order to determine how small or deep a defect has to be to be detected, a signal-to-noise-ratio analysis is used. This describes the relative contrast between a defect and its neighbourhood (Hidalgo *et al.*, 2013).

In order to compute this quantity, two distinct areas in the image are defined. One is the area over the defect taken as the signal and the other is the immediate vicinity of the defect as the noise. The two areas are illustrated in Figure 11 while Equation (5-3) was used to calculate the SNR.

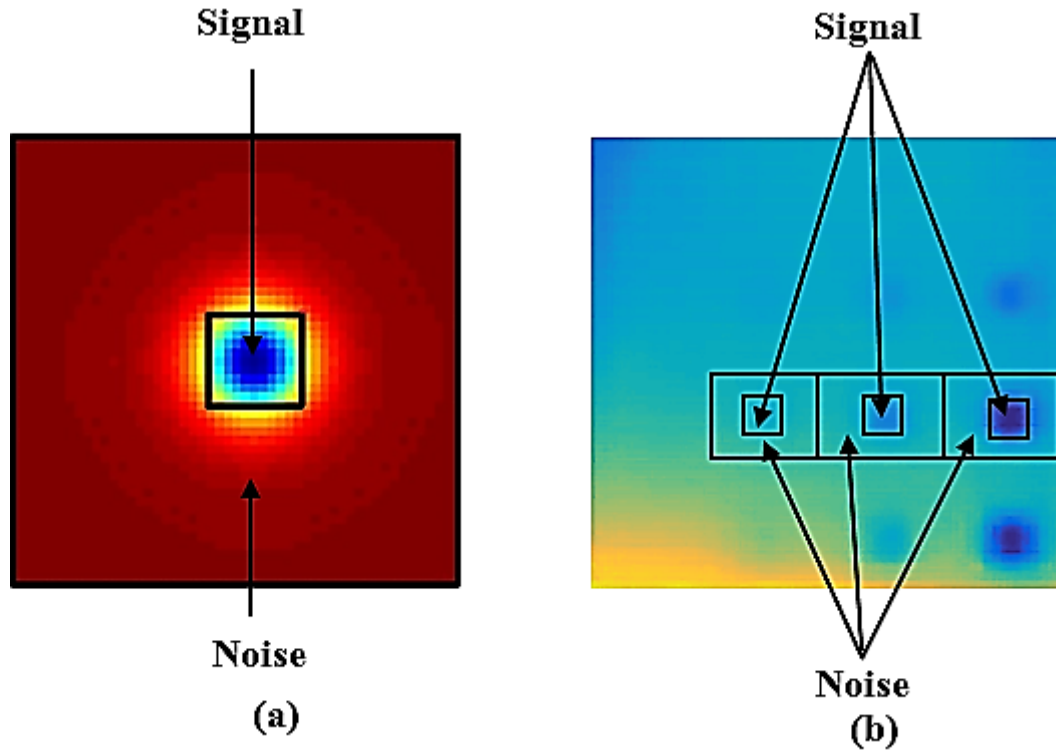


Figure 11: Areas considered as signal and noise for (a) Simulation and (b) experimental images

$$SNR = \frac{S}{N} 20 \log_{10} \left( \frac{abs(S_{mean} - N_{mean})}{\sigma} \right) \quad (5-3)$$

where  $\sigma$  is the standard deviation of the noise,  $S_{mean}$  is the mean of pixel values in the signal area and  $N_{mean}$  is the mean of pixel values in the noise area.

### 5.3 Surface Temperature Response

The temperature profile of the response signal has distinct characteristics compared to the input signal in that it has a d.c. component that results a consistent overall rise in temperature. In order to accurately obtain the phase information from the

signal using the Fourier transform, the a.c. component of the signal is processed (Junyan *et al.*, 2015). In order to obtain the a.c. signal, a linear curve is fitted to a response. Figure 12 shows the surface temperature response of a sample and a fitted curve to represent the d.c. component of the response while Figure 13 shows the response signal's a.c. component.

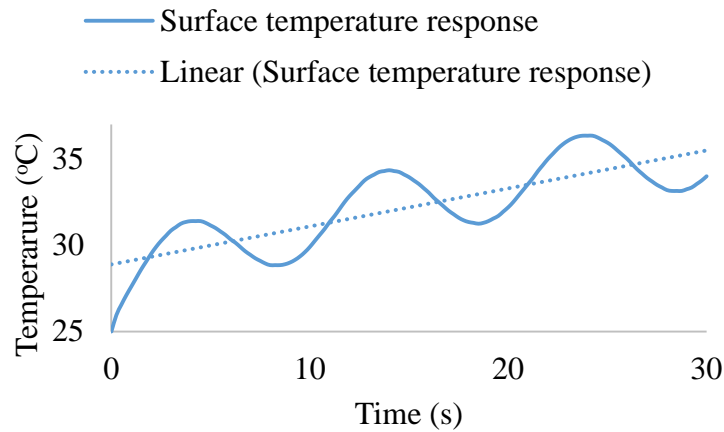


Figure 12: Typical surface temperature response and fitted curve representative of a d.c. component (Simulation data)

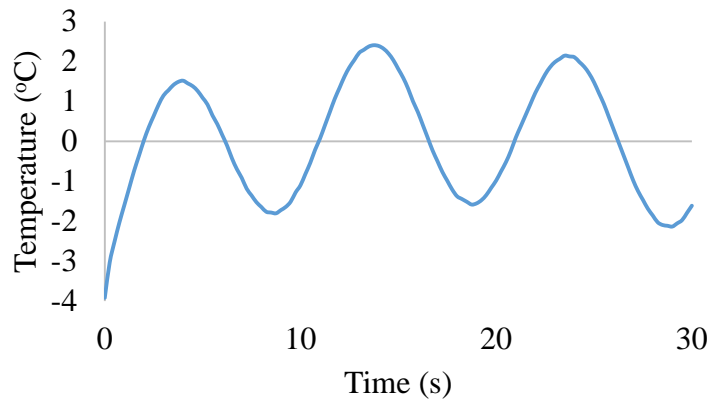


Figure 13: a.c. component of surface temperature response (Simulation data)

In order to obtain the a.c. component of the temperature response, also referred to as the thermal wave, a first order polynomial is fitted to the surface temperature response curve as shown in Figure 12. This polynomial as aforementioned represents the d.c. component of the temperature response and is then subtracted

from the surface temperature curve to obtain the a.c. component. This relationship is illustrated in Equation (5-4).

$$T_{ac}(t) = T_{sur}(t) - T_{dc}(t) \quad (5-4)$$

where  $T_{ac}(t)$  is the a.c. component of the temperature response,  $T_{sur}(t)$  is the temperature response and  $T_{dc}(t)$  is the d.c. component of temperature response.

## 5.4 Image Processing

The fast Fourier transform (FFT) was used to extract the phase of the surface temperature response of each pixel using MATLAB<sup>TM</sup> software. The phase values at the lockin frequency were obtained and converted into phase images. Phase images, as opposed to raw thermograms, are more suitable for viewing the defects as they enhance defect contrast. Processing involved three parts: a) d.c. component removal b) Fourier transform processing c) image construction. Removing the d.c. component, which rumps up the temperature of the sample, before processing was important as the Fourier transform produces errors when used on the raw temperature history data (Chatterjee *et al.*, 2011).

In processing data from the models, the temperature values were rounded off to the nearest 0.05°C so as to match the resolution of the infrared camera. The models had a resolution of 0.0001°C. The experimental data consisted of grayscale images that were representative of temperature. Therefore, in order to compare the temperature trends between the models and the experiments, these values were appropriately scaled and converted to temperature values using Equations (5-5) and (5-6).

$$I_{range} = I_{max} - I_{min} \quad (5-5)$$

$$T(x, y) = T_{min} + \frac{I(x, y) - I_{min}}{I_{range}} \times T_{range} \quad (5-6)$$

where  $I_{range}$  represents the range of grayscale intensity values of pixels in an image scene obtained by subtracting the lowest value from the highest. The temperature equivalent value,  $T(x, y)$ , to the grayscale,  $I(x, y)$ , at each pixel is obtained from

the minimum temperature  $T_{min}$  added to a fraction of the temperature range  $T_{range}$  in a scene. The temperature range is attained by deducting the minimum temperature value in the set range from the maximum.

## 5.5 Camera Noise

A brief study of the camera noise was conducted. This involved taking images of the sample without a stimulus applied to the surface for a period of time equal to experimental times. This was conducted in order to obtain information about the level of camera noise. Infrared camera manufacturers recommend that an infrared camera be calibrated every year to ensure precise measurements. This degradation in camera performance is attributed to electronic component aging ([www.flir.com](http://www.flir.com)). Figure 14 shows the temperature measurement fluctuations for a single pixel measured over a typical experiment duration with no applied excitation while Table 2 shows the average value of noise at each frequency.

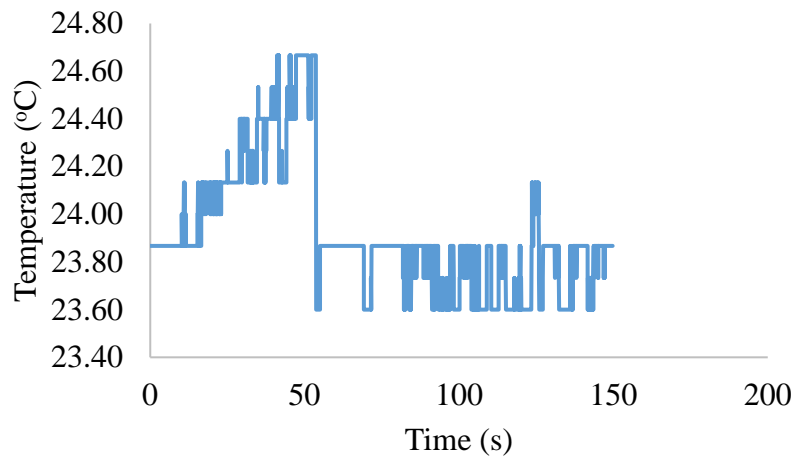


Figure 14: Camera temperature measurement variation with time

Table 2: Magnitude of noise recorded over time

Period (s)	Noise Magnitude (°C)	
	Carbon fibre	Steel
300	0.64	1.04
150	1.34	0.94
60	0.66	0.66
30	0.51	0.89
15	0.38	0.68
Average	0.71	0.84

### 5.5.1 Causes of Camera Errors

During analysis of experimental data, raw images are often not appropriate. Therefore after data acquisition, the thermograms are post-processed using image enhancement techniques to increase the signal-to-noise-ratio and defect clarity. Infrared images are degraded through a number of ways including vignetting, fixed pattern noise, dead pixels and radial distortion. Vignetting is defined as the darkening of image corners with respect to the centre. It is caused by the camera having a limited aperture and temperature variation between the lens and the scene. Fixed pattern noise is a noise pattern in digital imaging sensors often noticeable during long exposure shots and at very high temperatures where certain pixels give higher intensity values above the background noise. Dead pixels are pixels with incorrect intensity values caused by the detector having bad areas. To counter this problem, the dead pixel is replaced with the average value of the pixels surrounding it. Radial distortion relates to the image points with respect to the centre and may lead to noncollinear image points with respect to the optical centre. This is mainly dependent on the type of lens used (Ibarra-Castenado *et al*, 2004).

### 5.5.2 Simulation of Experimental Noise

This was conducted by applying random noise of varying amplitude to the shallowest and deepest defects temperature profiles for both carbon fibre and steel. Phase image results obtained indicated that the level of noise introduced affected the detectability of defects and deeper defects were more affected due to the low surface temperature contrast they induce which if too low matches experimental noise and the defect becomes undetectable. Steel was more affected than carbon fibre composite due the low overall temperature rise over the experiment and simulation frequencies. Simulations conducted at high frequencies experienced greater degradation effects when compared with ones at low frequencies. Both materials indicated that the effects of noise are greater at high frequencies. Figure 15 and Figure 16 moving from left to right show the degradation of the images with increase in noise peak-to-peak value for carbon fibre composite and steel respectively. Stand-alone images represent results obtained with noise free signals.

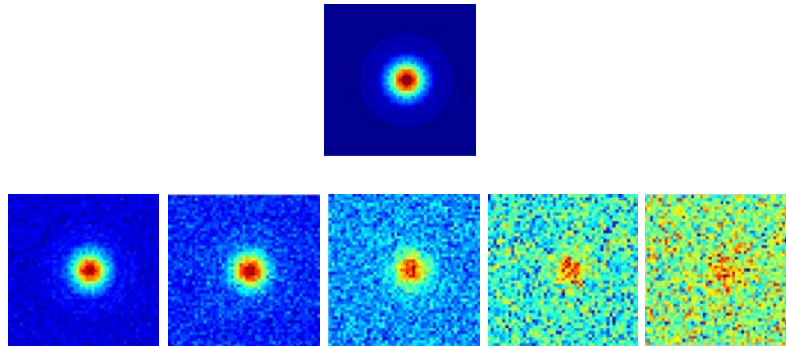


Figure 15: Simulation phase images for CFRP at 0.2 Hz with noise peak-to-peak values of 0.05, 0.1, 0.2, 0.5 and 1°C

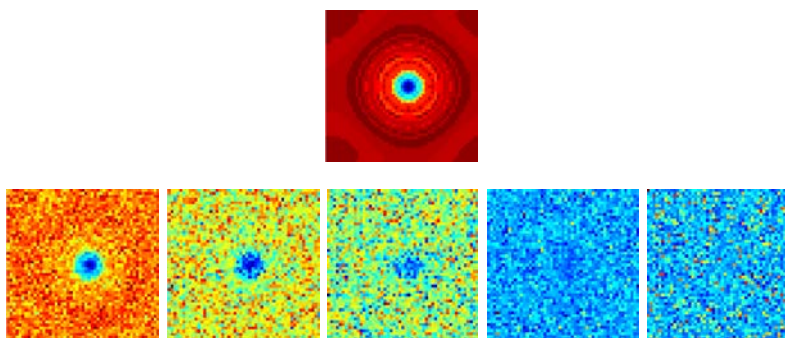


Figure 16: Simulation phase images for steel at 0.2 Hz with noise peak-to-peak values of 0.05, 0.1, 0.2, 0.5 and 1°C

## 5.6 Spatial Temperature Difference

A temperature difference between defective and nondefective areas is the basis of defect detection in infrared thermography. The higher the difference the more likely a defect is to be detected. In this regard, shallow defects exhibit higher thermal contrast compared with deep defects and as a result are easier to detect (Lahiri *et al.*, 2012). The same is true for defects with large areas when compared to ones with small areas.

But besides defect dimensions, other factors that affect the thermal contrast are the thermal conductivity and the specific heat. Materials with high thermal conductivity have greater lateral heat transfer rates than ones with low thermal conductivity which affects the phase contrast (Choi *et al.*, 2008). Also, materials with high heat capacities produce fairly low thermal contrasts for the same amount of energy deposited which results in a lower temperature rise. The thermal contrast is defined as the maximum temperature difference between the defective and the nondefective areas over the time history and is computed by Equation (5-7).

$$\Delta T(t) = T_d(t) - T_s(t) \quad (5-7)$$

where  $T_d$  is the temperature profile over the defective area and  $T_s$  is the temperature profile over the sound area all with respect to time. Thermal contrast plots for shallow and deep defects at a frequency of 0.01 Hz for carbon fibre and steel are shown in Figure 17 and Figure 18 respectively. The graphs show the variation in magnitude of thermal contrast of defects at different depths displaying the shallowest defects having the highest.

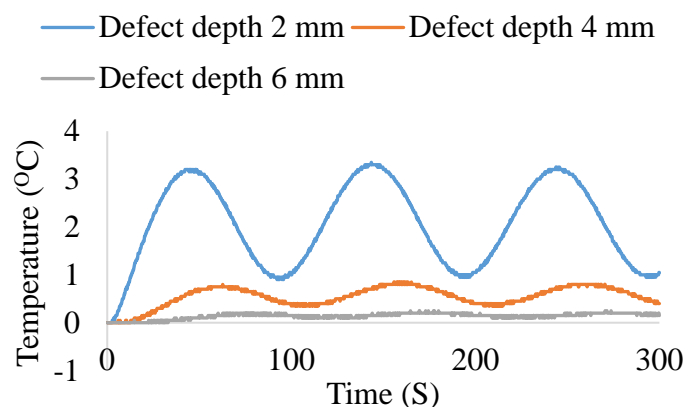


Figure 17: Defect thermal contrast at varying depths for CFRP (Simulated data)

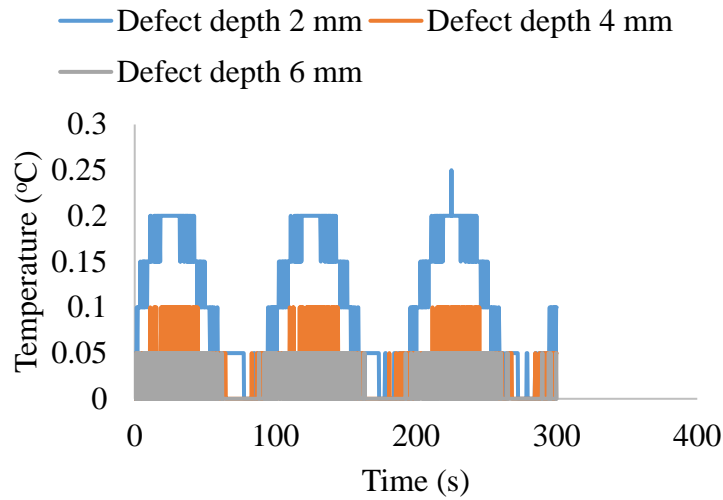


Figure 18: Defect thermal contrast at varying depths for steel (Simulated data)

## 5.7 Thermal Diffusion Length

The thermal diffusion length as discussed in section 2.3.1 is the depth at which the intensity of the excitation drops to  $1/e$  of that at the surface. It is a measure of the thermal wave's attenuation and represents the distance at which a significant decrease in the rate of heat transfer rate occurs. It varies for different materials as it is proportional to the thermal conductivity and inversely proportional to the specific heat. Another factor that affects the thermal diffusion length is the excitation frequency. The relationship between the aforementioned parameters is depicted by Equation (2-3) in section 2.3.9. For the two samples used, carbon fibre and steel, the thermal diffusion lengths at each excitation frequency implemented are presented in Table 3 and Table 4 respectively.

Table 3: Theoretically calculated thermal diffusion lengths for carbon fiber composite

Frequency (Hz)	Amplitude image		Phase image	
	Diffusion length	Detectable defect	Diffusion length	Detectable defect
	(mm)	(mm)	(mm)	(mm)
0.2	0.80	none	1.44	none
0.1	1.13	none	2.03	2
0.05	1.60	none	2.88	2
0.02	2.53	2	4.55	4
0.01	3.58	3	6.44	6

Table 4: Theoretically calculated thermal diffusion lengths for steel

Frequency (Hz)	Amplitude image		Phase image	
	Diffusion length	Detectable defect	Diffusion length	Detectable defect
	(mm)	(mm)	(mm)	(mm)
0.2	4.72	4	8.5	All
0.1	6.67	6	12	All
0.05	9.44	All	17	All
0.02	14.9	All	26.82	All
0.01	21.10	All	37.98	All

In order for a defect to be detected, its depth should be less than or equal to the thermal diffusion length (Chaterjee *et al.*, 2011). Furthermore, the probing depth for the phase image is 1.8 times more than the amplitude image (Moela *et al.*, 2013; Riegert *et al.*, 2006). For the same reason, it is thus possible to detect deeper defects at the same frequency with the phase image than with the amplitude image. Also, when compared with carbon fibre, it is thus possible to detect deeper defects at the same frequency in steel because its thermal diffusion length will be much higher.

## 5.8 Computed Tomography Scan

A CT scan was performed on the carbon fibre composite sample to ensure that it had no unknown defects. This would provide additional information on the technique with regards to its limitations. This was conducted at Stellenbosch University's Department of Wood Science CT scanner section that houses a General Electric VTomex L240 micro-CT and a Nanotom S nano-CT scanners. Scans were conducted using the micro-CT scanner as it is primarily suited to samples larger than 10 mm up to 300 mm along the longest axis while the nano-CT scanner is suited to samples less than 10 mm in diameter. The micro-CT scanner has a high power tube that allows voltages of up to 240 kV and high currents. This allows for more beam filtration and a sharper image with less beam hardening and other artefacts (du Plessis *et al.*, 2016). The results obtained exposed an air bubble approximately 1 mm in diameter located approximately 2 mm from the surface laying close to the 10 mm wide flat bottom hole. Besides this bubble, the rest of the sample was in good state and with only the fabricated defects present. Figure 20 shows CT scan images of the sample showing the position of the air bubble while Figure 20 shows the dimensions of the air bubble.

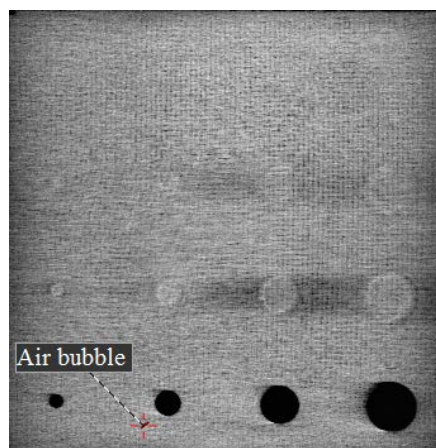


Figure 19: CT scan results showing position of air bubble

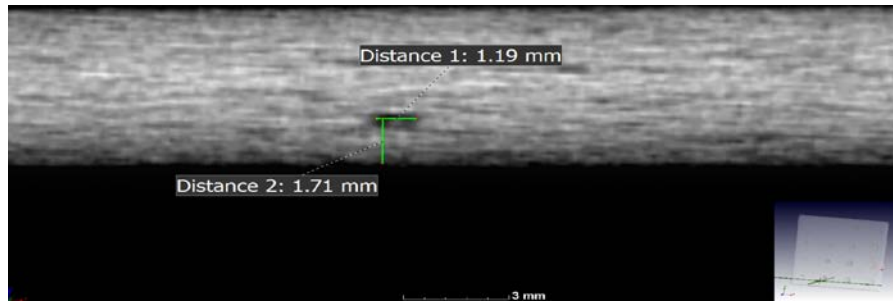


Figure 20: CT scan results showing cross section dimensions of air bubble

## 5.9 Chapter Summary

This chapter discussed the various analyses that were performed on the captured raw data. These were phase contrast and SNR definitions, image processing involving the fast Fourier transform, experimental and simulation noise, thermal contrast and thermal diffusion length definitions and CT scan results. The surface temperature response was pre-processed by removing the d.c. component from it to avoid erroneous results. A major note was that in materials with high heat capacity, the effect of experimental noise is much higher due to the low surface temperature rise. The thermal diffusion length is higher in materials of high thermal conductivity enabling quick inspection times as experiments can be accurately conducted in less time due to lower excitation wave cycle times. CT scan results revealed besides the inserted flat-bottom-holes, a 1.2 mm wide 1.7 mm deep air gap in the sample.

## 6 Influence of Excitation Frequency

This was an investigation of the extent excitation frequency affected defect detection. Five frequencies of 0.2, 0.1, 0.05, 0.02 and 0.01 Hz were selected with lamp peak power of 3000 W. An appreciable number of studies including one by Ghali *et al.* (2011) have investigated the influence of excitation frequency on the ability to detect defects. They all agreed that low excitation frequencies probe deeper into specimen. Therefore to probe deeper, the excitation must be carefully chosen to allow adequate diffusion of heat into the sample so as to reach the deep defects. Generally, in order to probe the entire thickness of the material, experiments are initially conducted at high frequencies to inspect the surface and shallow regions of the specimen and then continually decreased to inspect deep regions.

### 6.1 Carbon Fibre Composite

#### 6.1.1 Simulation Results

Simulation results for carbon fibre composite material are shown in Figure 21 for the set of frequencies 0.2, 0.1, 0.05, 0.02 and 0.01 Hz moving from left to right respectively. As one calls from Chapter three, the diameter of model defects in all cases was 10 mm. Phase image representations of the samples were selected for analysis due to their advantages over amplitude images that were discussed in section 2.3. At the highest frequency of 0.2 Hz, only the 2 mm and 4 mm deep defects were visible while the 6 mm deep defect was undetectable. This can be seen from the first column of the figure. As the frequency was lowered, the 6 mm deep defect became visible and the clarity improved. The change in colour of the defect at 0.01 Hz in label (a) was due to the lateral heat diffusion which resembled the pattern of the excitation, oscillating as the thermal wave was dispersed. The rate of lateral heat transfer that occurred was dependent on the excitation frequency as the amplitude of the wave was modulated. Therefore modulating the excitation intensity directly affected the lateral heat transfer in similar fashion.

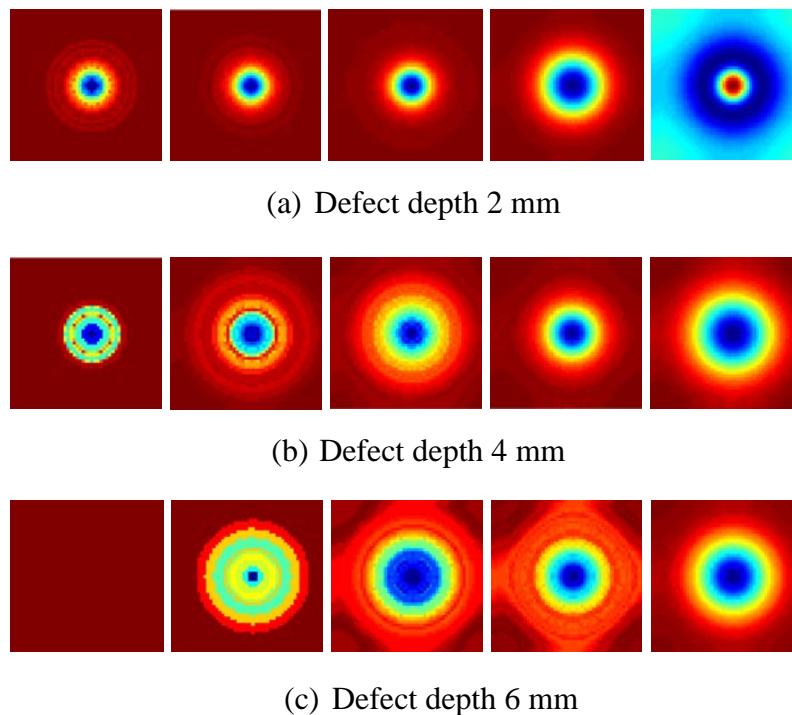


Figure 21: Carbon fibre composite simulation phase images at 0.2, 0.1, 0.05, 0.02 and 0.01 Hz

Also to note was that the thermal contrast for the 6 mm deep defect at 0.2 Hz was zero. That is to say that the thermal wave had not reached the defect over the experimental time window. Increasing the cycle time there by reducing the frequency advanced deep defect detection as the thermal wave diffused adequately through the material to reach the deep defects with sufficient intensity to cause a change in heat pattern detectable on the surface.

#### 6.1.1.1 Phase Contrast

Phase contrast measurements indicated a sign change between 0.2 Hz and 0.1 Hz, moving from positive to negative contrast value for the 2 mm deep defect. This indicated the presence of a blind frequency between the two values. For each defect, the blind frequency occurred at varied frequencies. Also, the deeper defects experienced more than one sign change over the range of frequencies used implying they had more than one blind frequency. The main difference between the frequencies used was that the phase contrast increased with reduction of excitation frequency. Then a maximum was reached and further reduction in frequency only resulted in a reduction in phase contrast for the 2 mm deep defect. The 4 mm and 6 mm deep defects had similar phase contrast trends to the other and to the 2 mm

deep defect over the range of frequencies studied except at the lowest frequency of 0.01 Hz where the phase contrast for the 2 mm deep defect reduced while for the 4 mm and 6 mm defects it was maximum. This is shown in Figure 22.

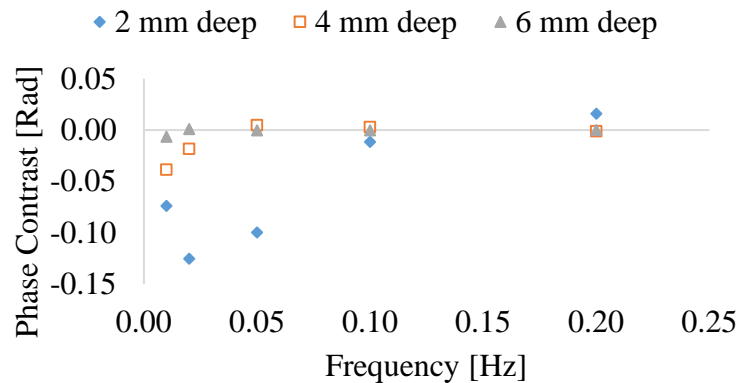


Figure 22: Phase contrast plot for carbon fibre composite with 3000 W excitation

### 6.1.1.2 Signal-to-Noise-Ratio

Signal-to-noise-ratio analysis for the 2 mm deep defect indicated a reduction in the SNR moving from high to low frequencies. The reduction in the SNR at lower frequencies was due to an increase in the defect size representation which indicates a bigger defect at lower frequencies. In as much as the defect is exposed, the error in size increases with a reduction of excitation frequency. From section 5.2, the signal area and the noise area remain the same but the mean of the noise area increases due to an increase in defect size representation. This increase in noise area mean combined with an increase in noise area standard deviation results in a reduction in signal-to-noise-ratio. At high frequencies, the heat flow is predominately one-dimensional as the exposure time is small. But as the cycle time is increased, more heat is introduced into the sample and as a result three dimensional effects increase. The SNR graphs at the depths investigated against excitation frequency are shown in Figure 23.

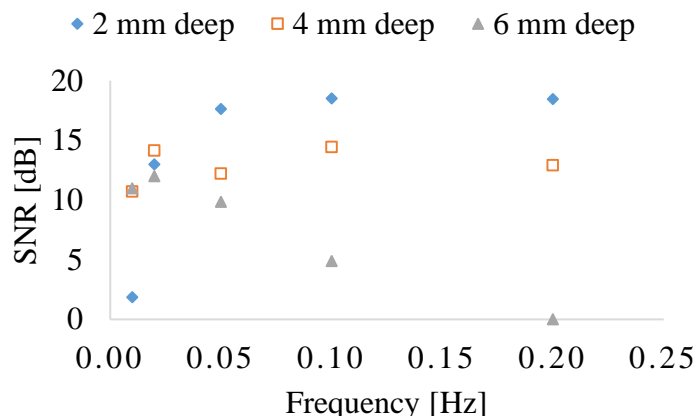


Figure 23: SNR for CFRP at varying defect depths vs frequency with 3000 W excitation intensity

For the 4 mm deep defect, the trend is similar to the 2 mm deep defect despite having an outlier at 0.05 Hz. This was thought to be due to an increase in heat being transferred away from the defect as depicted by the bright red ring around the defect in Figure 21. The 6 mm deep defect SNR rose from zero at the highest frequency as it was completely undetectable and reached maximum at 0.02 Hz. After which a further reduction in frequency resulted in a reduction of SNR.

### 6.1.2 Experimental Results

Experimental results also proved that the excitation frequency influenced the ability to detect deep defects. Lowering the frequency aided in the detection of deep defects. However, the deepest defect detected was at 4 mm from the surface in contrast to 6 mm in simulated data. It is worth mentioning that despite the 4 mm deep defects showing at 0.02 Hz, their contrast was poor. This improved as the frequency was lowered to 0.01 Hz. Furthermore, based on the thermal diffusion length calculations in section 5.3, the defects intended to be detected were revealed besides the 6 mm deep ones of all sizes. This was because the thermal contrast the defects produced was undetectable by the infrared camera. Phase images of experimental work conducted over the range of frequencies from 0.2, 0.1, 0.05, 0.02 and 0.01 Hz are shown in Figure 24. Moving from left to right in the very figure, the excitation frequency was reduced resulting in the deeper defects displaying. In the sample scene, defects on the far right were the shallowest and moving to the left

was an increase in defect depth. Therefore shallow defects revealed at higher frequencies than deep defects that revealed at lower frequencies.

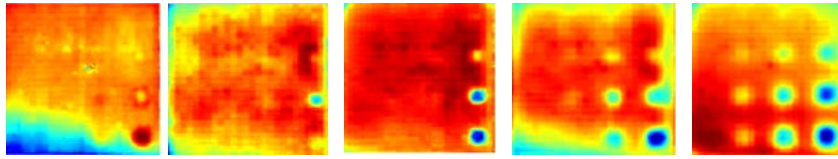


Figure 24: Experimental phase image results for carbon fibre composite at 0.2, 0.1, 0.05, 0.02 and 0.01 Hz

### 6.1.2.1 Phase Contrast

The trend of the phase contrast curve for the 2 mm deep defects closely resembled. A major difference was that the simulation values were higher. Further, at high frequencies the deep defects produced low phase contrast due to the high attenuation of heat through the material. This high heat attenuation makes detecting deep defects challenging as they produce low thermal contrast which for a defect to be detected has to be greater than the detector noise. The phase contrast variation with excitation frequency for the three defect depths is shown in Figure 25.

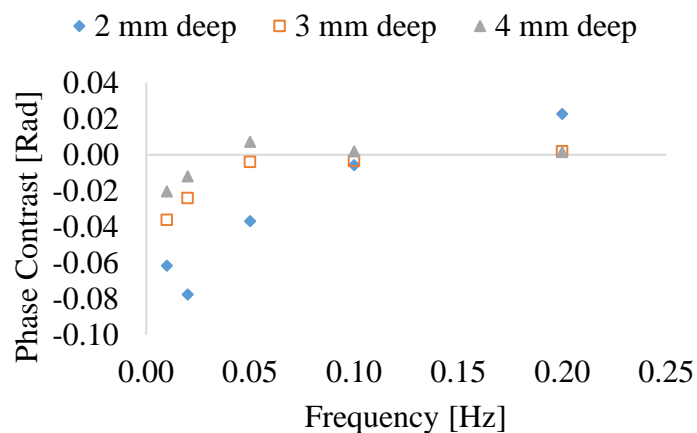


Figure 25: Carbon fibre composite experimental phase contrast variation with excitation frequency

A key note to make is that despite the 4 mm deep defect barely revealing at 0.02 Hz, the difference in phase contrast between the 2 and 4 mm defects is high. This reduced the clarity of the 4 mm deep defects. At 0.01 Hz, this difference in phase

contrast reduced due to the reduction of phase contrast by the 2 mm deep defect and a gain for the 4 mm deep defect. The reduction in the difference between the two values of phase contrast aided in the increase of clarity for the 4 mm deep defect.

### 6.1.2.2 Signal-to-Noise-Ratio

The SNR for the 2 mm deep defect was high at low frequencies. This was attributed to an increase phase contrast which increased the defect contrast from the sound region. For the 3 mm and 4 mm deep defects, the SNR values at high frequencies were not obtained as the defects were not visible on the phasegrams. At low frequencies where they were detected, the SNR increased as the defect became more vivid but the overall value was small. This is shown in Figure 26.

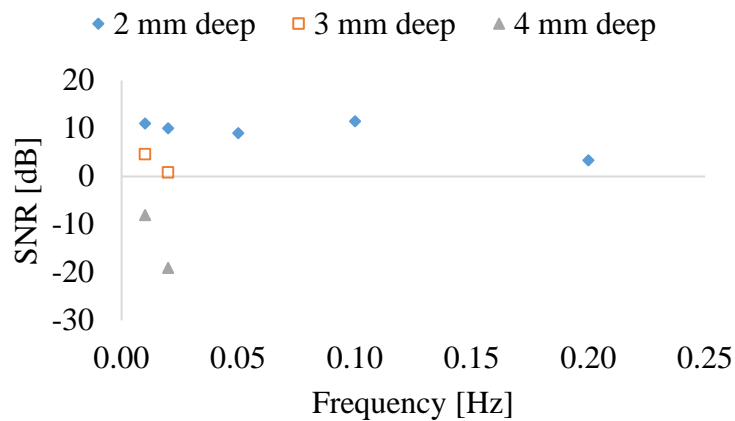


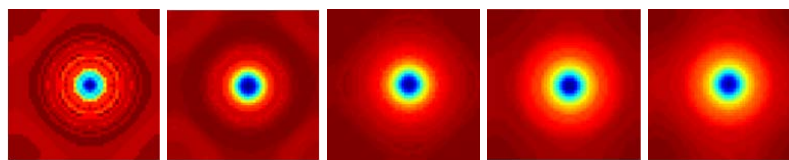
Figure 26: Carbon fibre composite SNR at varying defect depth

The SNR being a comparison between the strength of the defect signature and the sound area indicated that lower frequencies are favourable for detecting deep defects as they give better signal contrast enabling defect detection. This was true for all defects regardless of depth beneath the surface but was more pronounced for deep defect as they were undetectable at high frequencies.

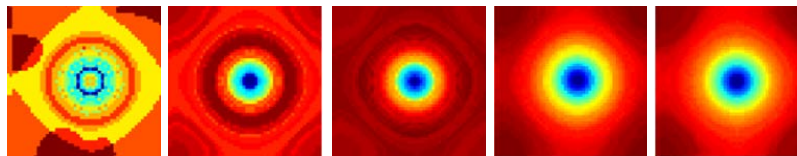
## 6.2 Steel

### 6.2.1 Simulation Results

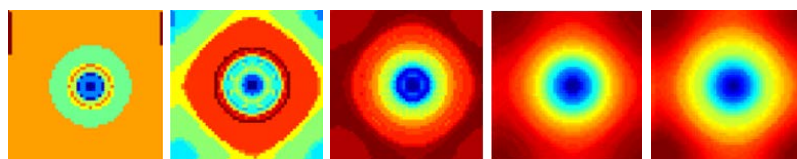
Like carbon fibre composite, lowering the frequency aided in the detection of deep defects in steel. However, steel being more thermal conductive than carbon fibre composite resulted in all defects being detected over the entire range of frequencies as the thermal wave was able to reach the deep defects quicker. This is the reason higher frequencies do not probe deep into materials with low thermal conductivity as the heat is highly attenuated and the amount that reaches the deep defects is insufficient to cause an irregularity in subsurface temperature distribution that can be detected from the surface. Figure 27 shows the variation in surface temperature response as the excitation frequency was lowered. In the images presented, defects at different depths are labelled with lowercase letters and moving from left to right across each row is a reduction in excitation frequency.



(a) Defect depth 2mm



(b) Defect depth 4 mm



(c) Defect depth 6 mm

Figure 27: Steel simulation phase images at 0.2, 0.1, 0.05, 0.02 and 0.01 Hz

A major difference between the images is the occurrence of lateral heat diffusion at different times especially notable at high frequencies. This indicates the difference in the rates of thermal attenuation for defects at different depths and materials with varied properties. For carbon fibre composite, the image at 0.2 Hz for the 6 mm

deep defect was different from steel as there was no indication of an underlying defect while it was visible in the steel simulation.

### 6.2.1.1 Phase Contrast

The phase contrast trend for steel once more was similar to carbon fibre for the shallow defects at 2 mm deep despite their maximum phase values occurring at distinct frequencies. The maximum contrast for steel occurred at 0.05 Hz and 0.02 Hz for carbon fibre composite. The 4 mm and 6 mm deep defects also experienced a disparity in the frequency that gave maximum contrast. A major observation was that the majority of the phase contrast values for steel were positive and so too was the maximum phase contrast value over the frequency range used in disagreement with carbon fibre composite which had most of its values and maximum phase contrast value negative. This phenomena is dependent on the defect properties with respect to sample material (Meola & Carlomagno, 2004). Figure 28 shows phase contrast variations for defects at depths of 2, 4 and 6 mm at varying frequencies.

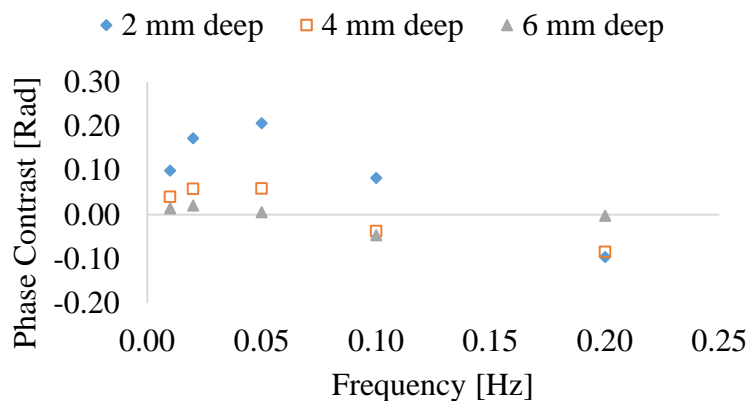


Figure 28: Phase contrast plot for steel at 3000 W

### 6.2.1.2 Signal-to-Noise-Ratio

The signal-to-noise-ratio trend in steel was similar to carbon fibre composite for the 2 mm deep defect reducing from high to low with a reduction of frequency. Notably for steel was that the values fall at a slower rate when compared to carbon fibre composite and as a result, the lowest value for steel was greater by a factor of three. As for the 4 mm and 6 mm deep defects, the strength of the signal rose steadily, reached a peak at 0.05 Hz after which it declined. The decline was attributed to a

high rate of lateral heat transfer due to the longer experiments at lower frequencies allowing for the material to reach for thermal equilibrium (Chatterjee *et al.*, 2011). SNR plots for defect depths of 2, 4 and 6 mm at varying excitation frequencies are shown in Figure 29.

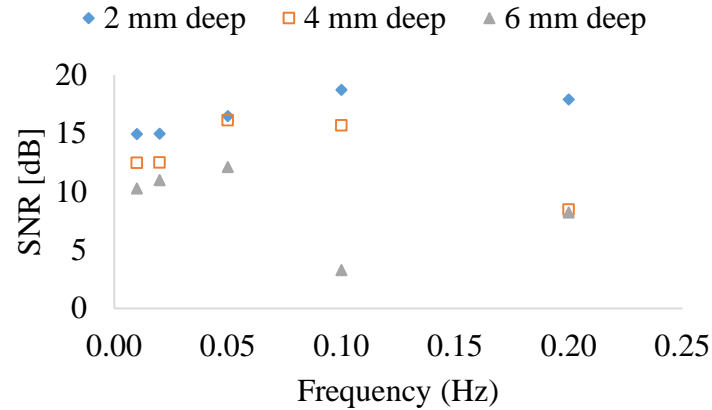


Figure 29: SNR for steel at varying defect depths vs frequency with 3000 W excitation intensity

In the case of the 6 mm deep defect, a major difference between steel and carbon fibre composite samples was that at the highest frequency of 0.2 Hz, the 6 mm deep defect was not visible in carbon fibre composite due to the higher attenuation of heat by the material while in steel it revealed.

## 6.2.2 Experimental Results

Experimental images showed that when the frequency was lowered, three-dimensional heat transfer effects increased reducing the defect contrast. This suggested that for materials with high thermal conductivity, high frequencies are more ideal as the rate of lateral heat transfer is less due short experiment times. The results differed from model data as models did not account for interaction of heat from other defects, being more pronounced in highly conductive materials. Also, the models were symmetric thereby having close range values for the amount of lateral heat transfer across each side of the defect. From the thermal diffusion length calculation, despite low frequencies having the ability to probe deeper in the material, there exist a limit where the rate of lateral heat transfer is significantly high for defects to be detected reliably. Studies conducted on mild steel were carried out

at high frequencies, 0.2 to 1 Hz and resulted in a maximum probed depth of 0.9 mm (Zimnoch *et al.*, 2010) compared with 0.01 to 0.2 Hz with a probable depth of 4 mm in this study. Phase contrast and SNR analysis were not conducted as the results obtained did not clearly reveal the defects under study at three of the five frequencies used. Figure 30 shows the phasegrams obtained over the frequency range 0.2 Hz to 0.01 Hz moving from left to right respectively.

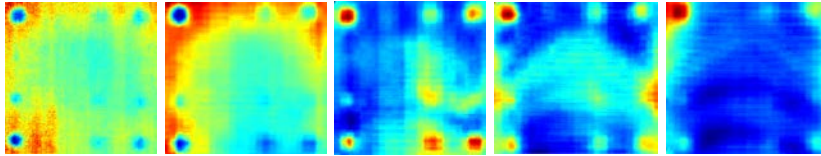


Figure 30: Experimental phase image results for steel at 0.2, 0.1, 0.05, 0.02 and 0.01 Hz

### 6.3 Chapter Summary

An overview of the notables in this chapter are presented, in simulation data the defect size representation differed with change of excitation frequency at a higher rate in the CFRP than in steel. This was due to a higher rate of lateral heat transfer in steel than carbon fibre composites that enables high rate of flow of heat away from the defective area. There was good correlation between simulation and experimental data showing the practical viability of lockin infrared thermography noted mostly for carbon fibre composite were deep defects up to 4 mm were revealed clearly. Shallow defects too in carbon fibre composite were readily detectable and showed high rate of phase contrast increase with reduction of excitation frequency.

## 7 Influence of Excitation Number of Wave Cycles

This was a comparison between using three and five wave cycles of the excitation. In literature there is mention of more wave cycles increasing the signal-to-noise-ratio of the defects (Ibarra-Castanedo *et al.*, 2005; Duan *et al.*, 2013). The extent having more wave cycles influenced results was investigated. As is expected, increasing the number of wave cycles increased experiment and simulation times and so too the total amount of energy injected into the sample. The surface temperature responses of the sample are shown in Figure 31. It should be noted that the five excitation wave cycles surface temperature response wave is exactly the same as the three cycle one only that it extends further. The waves shown in the graph represent surface temperature responses to a thermal wave of pixels from defective (five cycles) and sound (three cycles) regions.

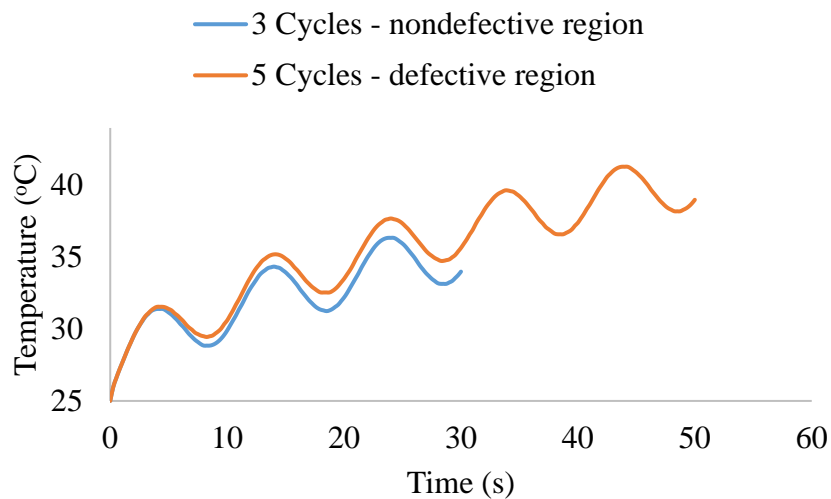
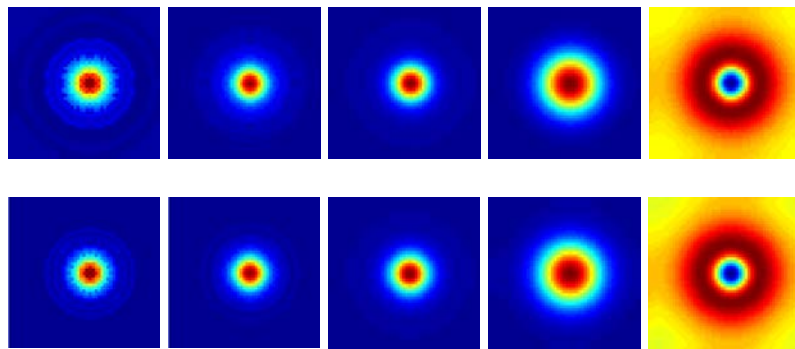


Figure 31: Simulation data surface temperature results for CFRP at 0.1 Hz over defective and nondefective regions

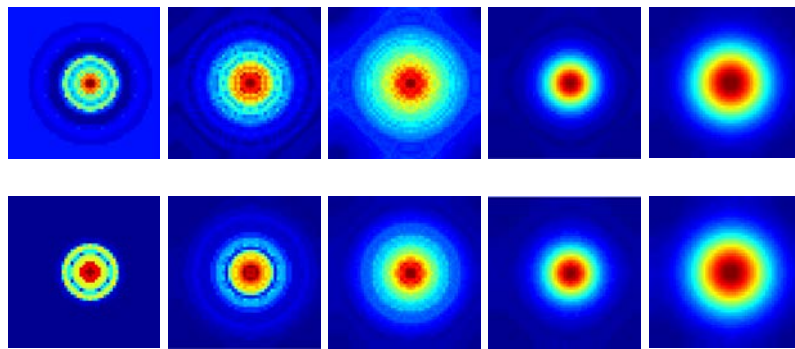
## 7.1 Carbon Fibre Composite

### 7.1.1 Simulation Results

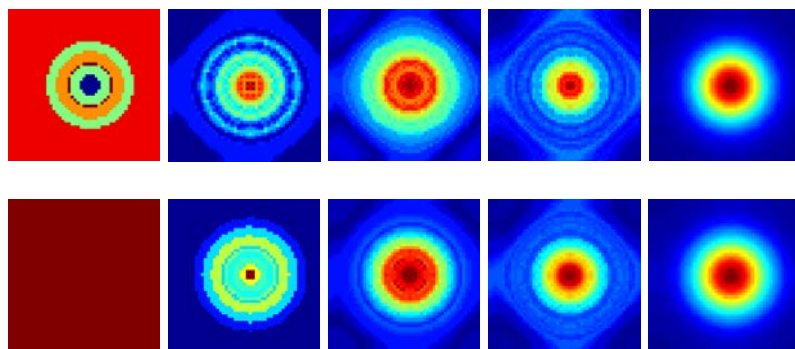
A major difference noted between using three wave cycles against five was that size of the rings around the defects was smaller at high frequencies while using three cycles for all defects. This was an indication of low rates of lateral heat transfer, the dominant phenomena being one dimensional heat transfer at high frequencies. Using five cycles extended the heat exposure time which increased the amount of energy introduced into the test sample. Therefore it was important to note the optimum frequency at which the defects had a fair balance between one dimensional and three dimensional heat transfer modes in order to produce the highest phase contrast and SNR. Model images for carbon fibre composite are presented in Figure 32 showing a comparison of images obtained from using five cycles (top images) and three cycles (bottom images) for Figures 7-2 a, b and c. Moving across each row from left to right is reduction of excitation frequency from 0.2, 0.1, 0.05, 0.02 and 0.01 Hz respectively.



(a) Defect depth 2 mm



(b) Defect depth 4 mm



(c) Defect depth 6 mm

Figure 32: Comparison CFRP simulation images obtained from using 5 (top) and 3 (bottom) cycles for defects at varying depths

It was noted in (a) that as the excitation frequency was reduced, the size of the defects appeared to increase in size in both instances. This was attributed to the high rates of lateral heat transfer associated with the increase in exposure time and energy. The two cases for the 2 mm deep defect showed a correlation as they both exhibited this increase. For the 4 and 6 mm deep defects, defect clarity increased

significantly with reduction of excitation frequency at similar rates showing little dependence on the number of excitation wave cycles.

### 7.1.1.1 Phase contrast

The phase contrast was noted to be slightly higher at all frequencies besides 0.2 Hz after using five wave cycles for 2 mm deep defect while at 0.2 Hz, using three wave cycles produced better phase contrast. This is shown in Figure 33 for the 2 mm deep defect while Figure 34 shows a slightly different trend for the 4 mm deep defect. The phase contrast was higher from using three wave cycles than from using five.

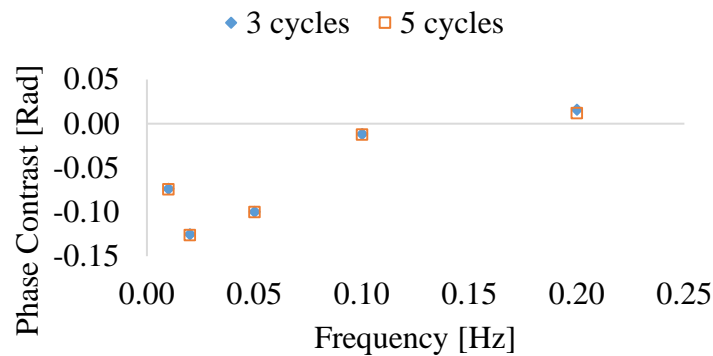


Figure 33: Phase contrast plot for 3 and 5 cycles at 2 mm deep

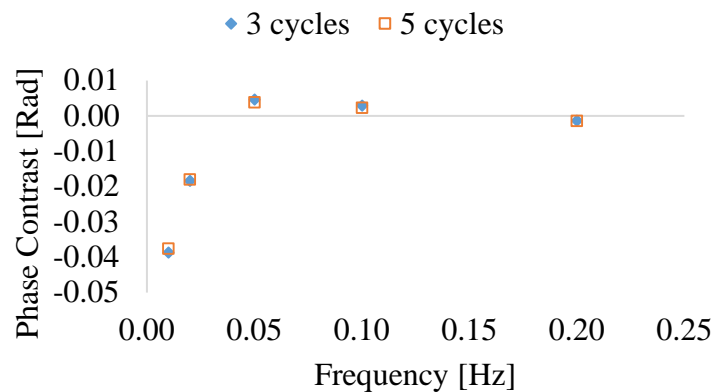


Figure 34: Phase contrast plot for 3 and 5 cycles at 4 mm deep

For the 6 mm deep defect, the phase contrast curve had more than one blind frequency. The overall phase contrast was low compared with the 2 mm deep defect

by factors of 11 times less and 7 times less with the 4 mm deep defect. Therefore, despite the defect being clearly visible in simulation results and showing an increase in phase contrast at low frequencies, this defect would be difficult to detect in experimental data due to its low value unless capturing the raw data using a camera with high resolution and frame rate. The phase contrast plot for the 6 mm deep defect is shown in Figure 35.

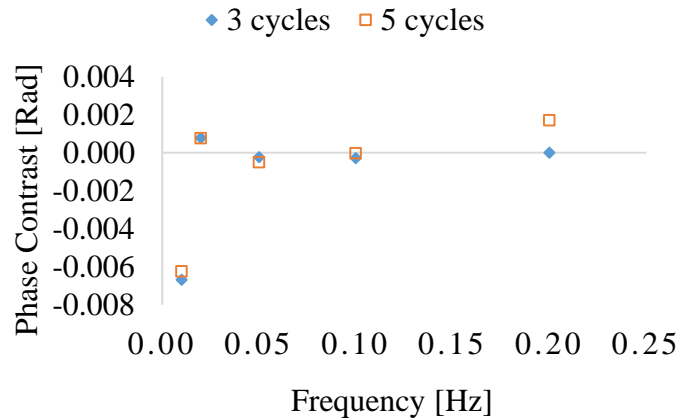


Figure 35: Phase contrast plot for 3 and 5 cycles at 6 mm deep

The phase contrast graph for the 6 mm deep defect had a similar trend to the 4 mm deep defect where using five wave cycles produced a slightly higher phase contrast values except at 0.2 Hz. That is using five cycles produced a higher phase contrast for most of the frequencies used. Further, the 6 mm deep defect was not visible at 0.2 Hz from using three wave cycles, but revealed from using five wave cycles.

### 7.1.1.2 Signal-to-Noise-Ratio

Using three wave cycles produced slightly higher SNR values at frequencies of 0.2 Hz and 0.1 Hz while the contrary was observed from 0.05 Hz down to 0.01 Hz for the 2 mm deep defect. A notable difference between the two was the steady increase in SNR values when using five wave cycles, having a maximum value at 0.05 Hz as opposed to a maximum at 0.1 Hz when using three cycles. In all, there was an insignificant amount of improvement from using three against five wave cycles as the trend was generally similar and the values were in the same range. A plot of the trends while using three against five wave cycles is shown in Figure 36.

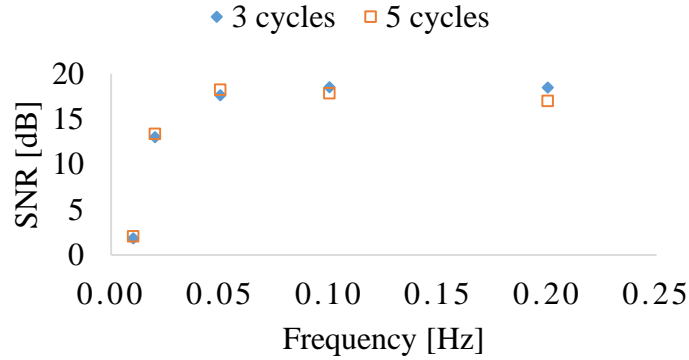


Figure 36: SNR for steel at for 2 mm deep defect vs frequency for 3 and 5 wave cycles

The SNR for the 4 mm deep defect exhibited similar behaviour to the 2 mm deep defect in that at higher frequencies, using three wave cycles produced better SNR than using five cycles. The trends of the two plots had similar patterns and the maximum value for both in this case was at 0.02 Hz. As was the case with the 2 mm deep defect, varying the number of wave cycles from three to five had an insignificant effect on the SNR. The SNR plot for the 4 mm deep defect while using three and five wave cycles is shown in Figure 37.

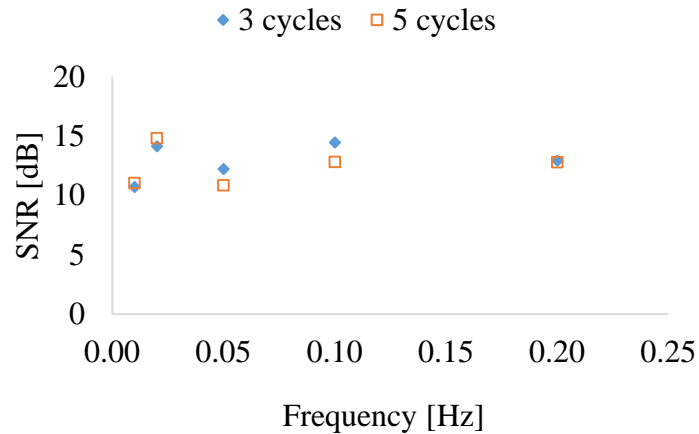


Figure 37: SNR for steel at for 4 mm deep defect vs frequency for 3 and 5 wave cycles

As for the 6 mm deep defect, by virtue of the defect not being visible at 0.2 Hz produced zero value of SNR with applying three excitation wave cycles. The SNR rose with a reduction of frequency and attained a maximum value at 0.02 Hz then

fell again at 0.01 Hz. With using five wave cycles, the trend alternated between increasing and decreasing values, reaching a maximum at 0.02 Hz. Both cases had maxima at 0.02 Hz and the values were within 0.75 dB of each other with application of five wave cycles producing the upper value. Despite the large difference in trend, both defects in practical terms would not be detected unless with a highly sensitive system due to their low phase contrast values at higher frequencies. A plot of the SNR for the 6 mm deep defect is shown in Figure 38.

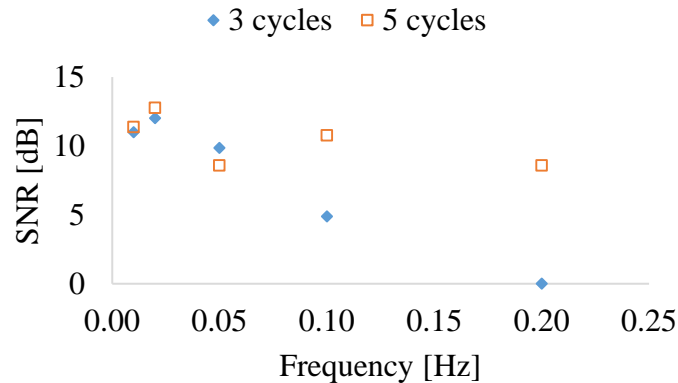
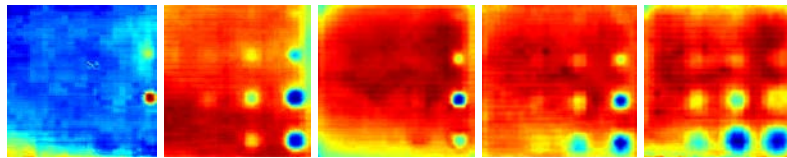


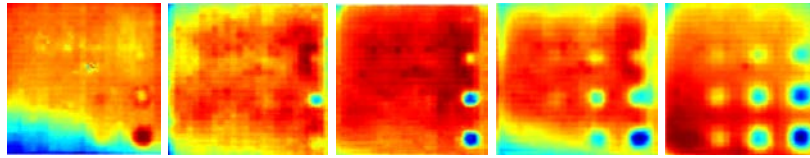
Figure 38: SNR for steel at for 6 mm deep defect vs frequency for 3 and 5 wave cycles

### 7.1.2 Experimental Results

There was reduction in image noise from using five wave cycles as opposed to three and this is shown in Figure 39. There was an outlier at 0.1 Hz where experimental results revealed the deepest detectable defect at 3 mm deep when using five wave cycles while only the 2 mm deep defects were visible from using three cycles. The reason behind this anomaly was not investigated further. In the displayed images below, moving from left to right is a reduction in excitation frequency from 0.2, 0.1, 0.05, 0.02 and 0.01 Hz respectively.



(a) Phase images of CFRP after five wave cycles



(b) Phase images of CFRP after three wave cycles

Figure 39: CFRP phase image results after using 5 wave cycles against 3 at 0.2, 0.1, 0.05, 0.02 and 0.01 Hz

### 7.1.2.1 Phase Contrast

The phase contrast trends were similar but the rate of increase and decrease was higher when using five cycles. Also, using five wave cycles produced higher phase contrast values than using three for all frequencies besides 0.01 Hz for the 2 mm deep defect. The overall phase contrast was sufficiently high for all but one frequency of 0.01 Hz. This showed the dependence of noise and lateral heat transfer on defect detection. Increasing the number of wave cycles increased the defect contrast as it reduced the effect of experimental noise. This observation was also made by Duan *et al.*, (2013). Variation of phase contrast with frequency for three and five excitation wave cycles are shown in Figure 40.

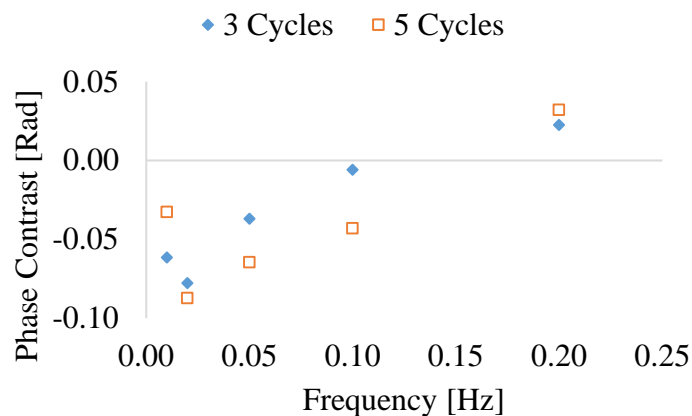


Figure 40: Phase contrast from using 3 against 5 excitation wave cycles

### 7.1.2.2 Signal-to-Noise-Ratio

The SNR was considerably lower at the lowest frequency with using five wave cycles as opposed to three by a factor of three. This was unusual as the difference in SNR values between the two excitation wave cycle variations was within a 3 dB range for all frequencies except 0.01 Hz where the difference between the two values was significantly higher than other frequencies. Using five wave cycles had maximum and minimum SNR at 0.02 Hz and 0.01 Hz respectively which corresponded to the frequencies at which the phase contrast was maximum and minimum respectively. This difference in values was attributed to an increase in phase variable range caused by wider defects in the image scene. Wider defects have higher phase contrast values than the narrow ones and their rate of increase is higher.

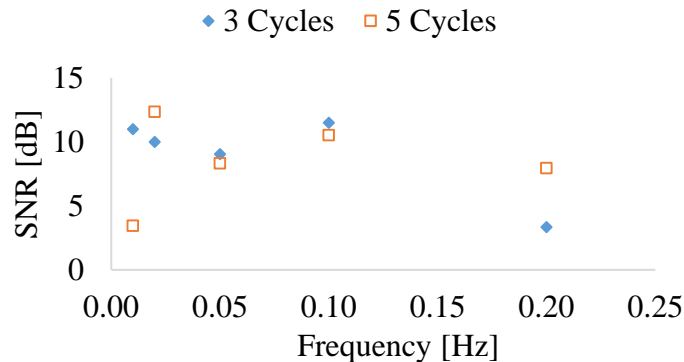


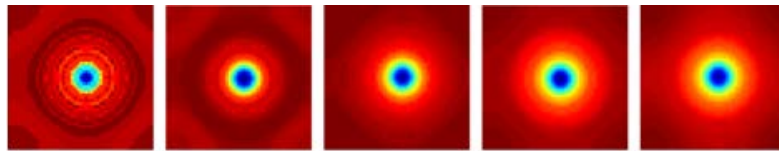
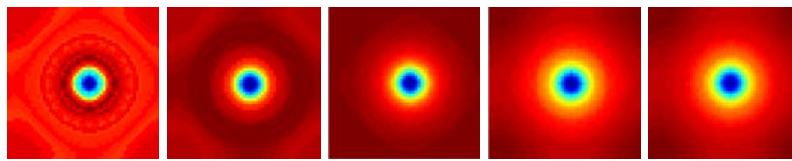
Figure 41: Experimental SNR plot for 2 mm deep defect

## 7.2 Steel

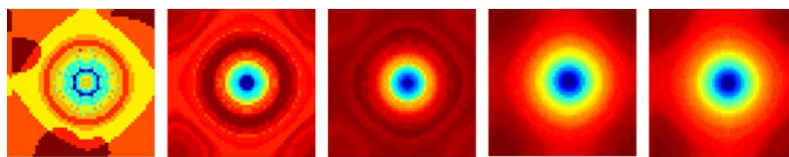
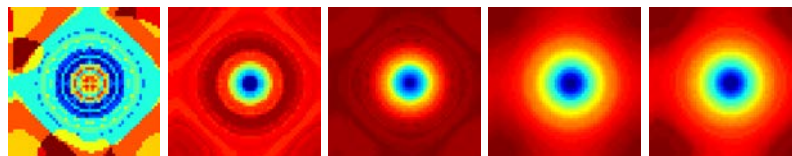
### 7.2.1 Simulation Results

In simulation data, a significant observation was made for the 6 mm deep defect at 0.2 Hz after using three wave cycles. The rings around the defect were not as spread out as ones obtained from using five wave cycles. This was due to more heat being injected into the sample resulting in more lateral heat transfer. Further, as the frequency was reduced, the two image results from using three and five wave cycles were similar as they both were able to show the defect despite the defect size representation being slightly different. The phasegrams of the defects are shown in

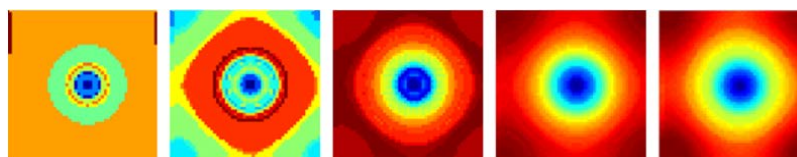
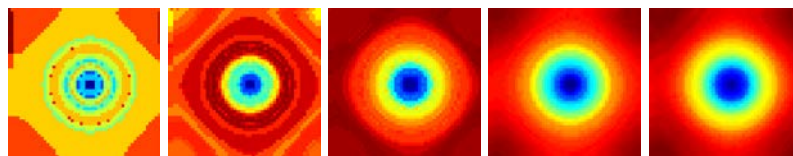
Figure 42 showing images obtained after using five wave cycles (top) and three (bottom) for Figures 42 a, b and c. Moving from left to right across each row is the reduction in excitation frequency from 0.2, 0.1, 0.05, 0.02 and 0.01 Hz.



(a) 2 mm deep defect



(b) 4 mm deep defect



(c) 6 mm deep defect

Figure 42: Comparison of steel simulation images obtained from using 5 (top) and 3 (bottom) waves cycles at varied defect depths and frequencies of 0.2, 0.1, 0.05, 0.02 and 0.01 Hz

### 7.2.1.1 Phase contrast

The phase contrast trend for the 2 mm deep defect was similar to carbon fibre composite with five cycles producing a slightly higher phase contrast. A similar trend was also observed for the 4 mm deep defect except at 0.05 Hz where the phase contrast was higher when using three cycles. That is four of the five frequencies used resulted in a higher phase contrast value when using five cycles. For 6 mm deep defect, there was no fixed pattern as at some frequencies using 5 cycles produced a higher phase contrast than using 3 cycles. This is as shown in Figure 43 below.

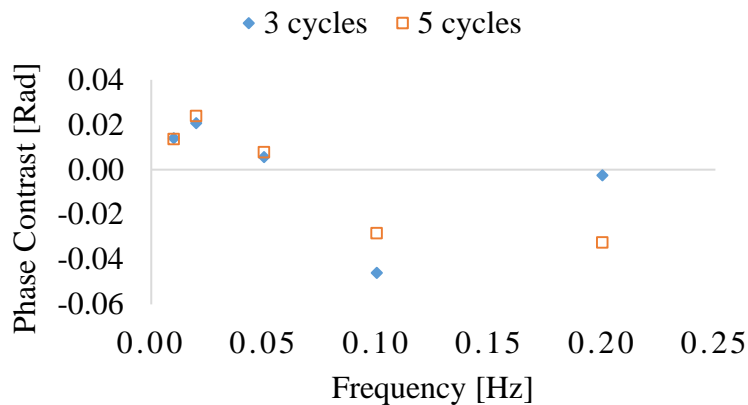


Figure 43: Phase contrast plot for 3 and 5 cycles for 6 mm deep defect

### 7.2.1.2 Signal-to-Noise-Ratio

Signal-to-noise-ratio comparison showed like trends between the two wave cycles for the 2, 4 and 6 mm deep defects. These values were significantly high over the entire range of frequencies used pointing to a high probability of detecting the defects from using either three or five wave cycles. A difference noted was the value being negative for the 4 mm deep defect at 0.2 Hz when using five wave cycles. This indicated that the defect footprint on the image was weak despite having a high phase contrast value. Comparing the phase response after using three wave cycles at 0.2 Hz against five, the result suggested a high possibility of errors at high frequencies due to the high rate of heat diffusion in steel. This may lead to false SNR readings. The SNR for the 2 and 4 mm deep defects are shown in Figure 44 and Figure 45 respectively.

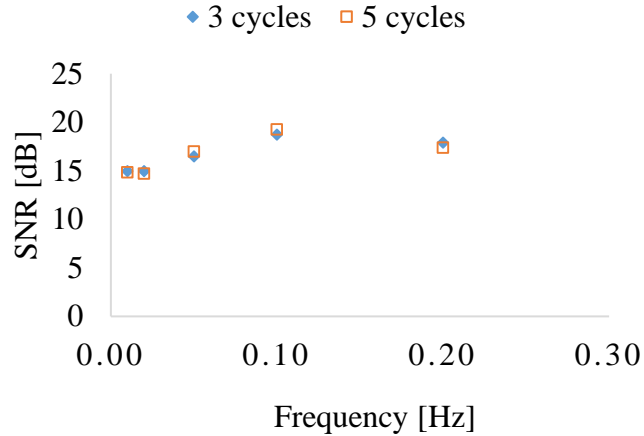


Figure 44: SNR plot for 2 mm deep defect

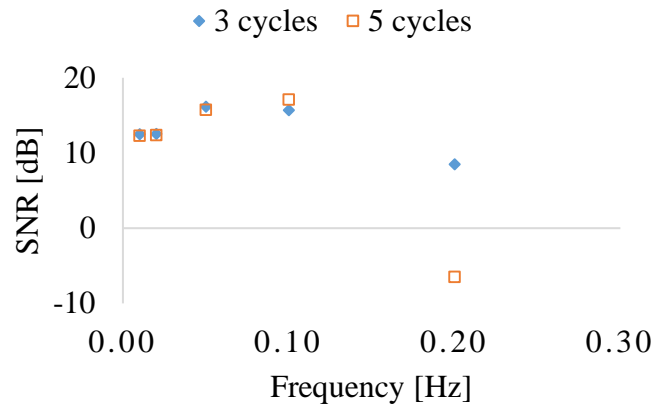
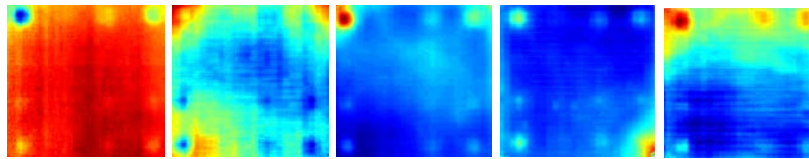


Figure 45: SNR plot for 4 mm deep defect

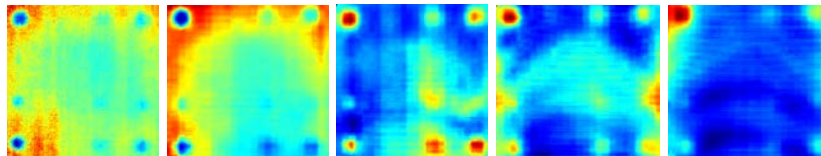
## 7.2.2 Experimental Results

Phase image representation of the results showed great variation with regards to defect clarity between using five wave cycles against three. Using five excitation wave cycles produced the better image contrast across the frequencies used. Also, the image noise appeared to be less from using five cycles at 0.2 Hz. The 10 mm deep defects were clearer and the surface temperature distribution was more uniform. This was also the case at 0.05 Hz and 0.02 Hz where the images appeared smoother and the individual defects distinct. After using three excitation wave cycles, the best results were at 0.2 Hz where the larger defects were revealed with appreciable clarity. In the case of the 10 mm wide defect, it was just visible enough

at 0.2 Hz and worsen as the frequency was lowered. Phase image results obtained from using three or five excitation wave cycles are shown in Figure 46.



(a) Phase images of steel after five wave cycles



(b) Phase images of steel after three wave cycles

Figure 46: Steel phase image results after using 5 wave cycles against 3 at 0.2, 0.1, 0.05, 0.02 and 0.01 Hz

### 7.2.2.1 Phase Contrast

Phase contrast analysis was conducted only for five wave cycles as the defect dimension under investigation was not easily distinguishable in experimental results obtained whilst using three excitation wave cycles. Therefore phase contrast analysis was with simulation data with five excitation wave cycles. The phase contrast trend matched with simulation data, being negative at high frequencies, changing sign with decrease in frequency, reaching maximum and falling with further decrease in frequency. A key difference between simulation and experimental data was that at the lowest frequency of 0.01 Hz, in experimental data the defect exhibited low phase contrast with respect its surrounding pixels. Phase contrast plots comparing simulation and experimental data are shown in Figure 47.

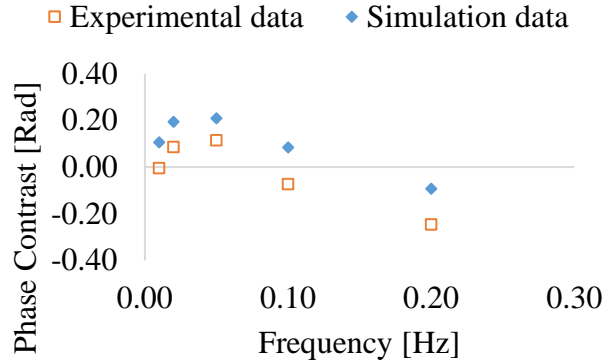


Figure 47: Steel phase contrast comparison between experimental and simulation data with 5 excitation wave cycles

### 7.2.2.2 Signal-to-Noise-Ratio

As was in the case with phase contrast, this comparison was conducted between experimental data and simulation data when five wave cycles were applied. The results obtained showed simulation data having higher SNR than experimental data for all frequencies used. In experimental data, the frequency at which the highest SNR occurred, 0.05 Hz, corresponded to the frequency at which the maximum phase contrast was obtained. This trend was important as it enables the determination of a frequency range that produces the least noise for enhancement of defect detection.

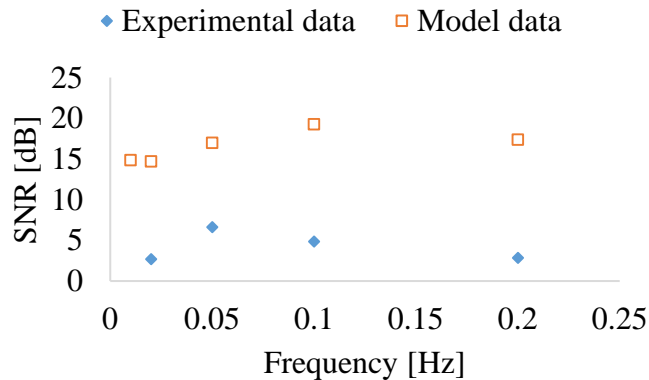


Figure 48: SNR comparison between simulation and experimental data

### 7.3 Chapter Summary

This chapter highlighted that an increased number of excitation wave cycles enhancement defect detection in experimental study for both carbon fibre composite and mild steel. The improvement was most pronounced in mild steel as using three wave cycles produced noisy results. In carbon fibre composite, using five wave cycles yielded acceptable results over the range of frequencies 0.2 – 0.02 Hz while at the lowest of 0.01 Hz the defect contrast for the 10 mm wide defect significantly reduced. This was attributed to the high rates of heat transfer that resulted from the increase in experiment time. The SNR in experimental data when using five wave cycles on both carbon fibre composite and steel were significantly high suggesting a high probability of defect detection. Experiment results on carbon fibre composite showed a dependence of the image clarity on the number of excitation wave cycles introduced to the sample surface at high frequencies. Using five excitation wave cycles revealed more defects at 0.2 and 0.1 Hz than using three cycles.

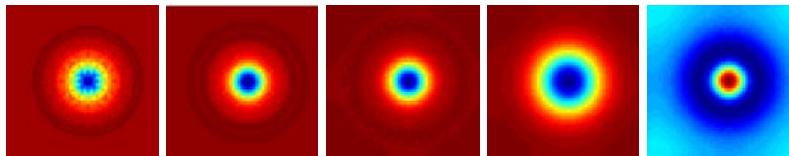
## 8 Influence of Excitation Power

Defect detection capabilities of lockin thermography depend on the power of the excitation among other factors (Ranjit *et al.*, 2015; Zoeke *et al.*, 2010). Phase noise is high when the amount of heat absorbed per unit area by the specimen is low. Therefore this study was focused on exploring the effect of the excitation intensity on defect detection. Three distinct intensities of 1500 W, 3000 W and 6000 W were used with frequencies 0.2, 0.1, 0.05, 0.02 and 0.01 Hz for both carbon fibre composite and steel samples.

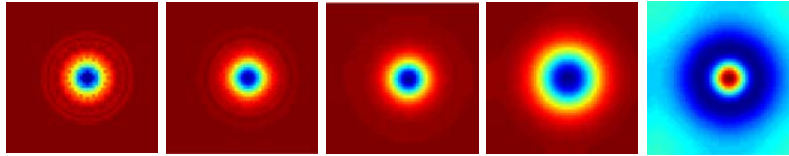
### 8.1 Carbon Fibre Composite

#### 8.1.1 Simulation Results

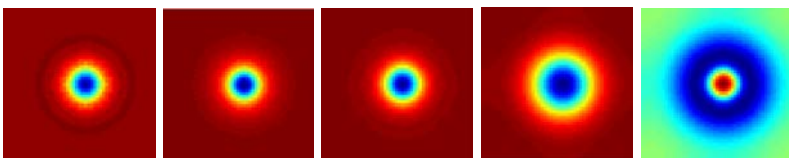
Varying the intensity had a significant difference on the phasegrams obtained at high frequencies. Phase images obtained at 0.2 Hz showed the defect clarity significantly increased with intensity increase. Images obtained at low frequencies showed little variation as the defect representation trend was similar. Another note was that the defect changed colour at 0.01 Hz in all cases. The reasons for this were as explained in section 6.1.1 due to variation in lateral heat transfer rates, the rate of lateral heat transfer varies accord to the excitation frequency, being higher and lower with respect to the reference signal. To support this, the phase contrast values were still negative indicating the phase contrast trend had not crossed the frequency axis to warrant change of defect phase contrast sign and hence colour (Moela & Carlomagno, 2004). For the 2 mm deep defect, Figure 49 shows phase image results obtained at varying intensities at frequencies of 0.2, 0.1, 0.05, 0.02 and 0.01 Hz respectively.



(a) Lamp intensity 1500 W



(b) Lamp intensity 3000 W



(c) Lamp intensity 6000 W

Figure 49: Carbon fibre composite phase images for 2 mm deep defect at 0.2, 0.1, 0.05, 0.02 and 0.01 Hz at varying excitation power intensities

### 8.1.1.1 Phase Contrast

Simulation phase contrast plots for carbon fibre composite revealed similar trends for all intensities. For the 2 mm deep defect, slight improvements in the phase value was noticed at 0.02 Hz and 0.01 Hz with 6000 W peak power. Increasing the frequency to 0.05 Hz, using a lamp intensity of 1500 W produced the greatest defect phase contrast. At the two highest frequencies of 0.1 Hz and 0.2 Hz, using 3000 W of power yielded the highest phase contrast values. It should be noted however that despite the three distinct lamp intensities giving better phase contrast results at specific frequencies, the improvement was only slight. Phase contrast plots for the 2 mm deep defect at frequencies of 0.2, 0.1, 0.05, 0.02 and 0.01 Hz are shown in Figure 50.

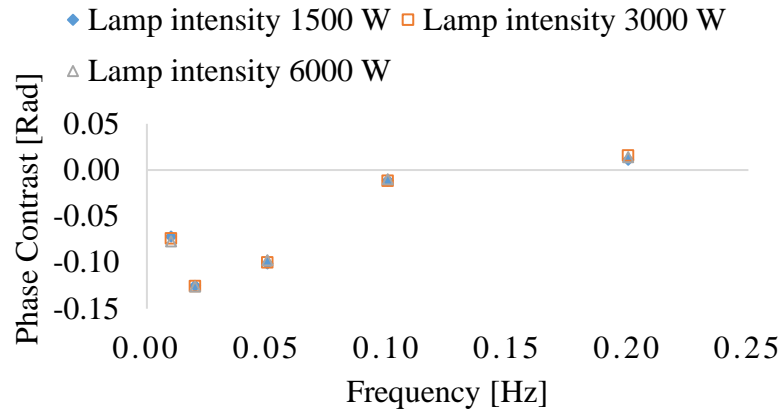


Figure 50: Phase contrast plot for 10 mm diameter defect 2 mm from the surface

### 8.1.1.2 Signal-to-Noise-Ratio

All three intensities had similar trends, having highest SNR values at high frequencies and lowest at low frequencies. At 0.01 Hz, the SNR value when using 6000 W was negative which could signify that in the phase image, pixel values of nondefective areas were higher than over defective areas due to the variation in lateral heat transfer occurring in the sample. Figure 51 shows plots of SNR vs excitation frequency for the 2 mm deep defect at 1500, 3000 and 6000 W.

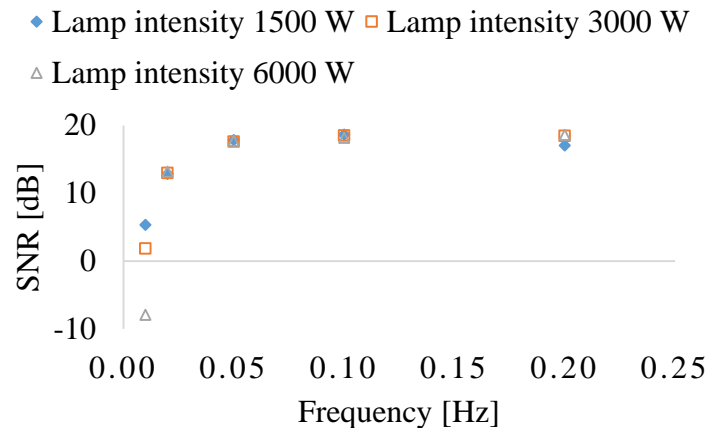
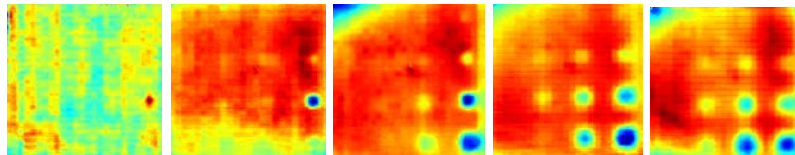


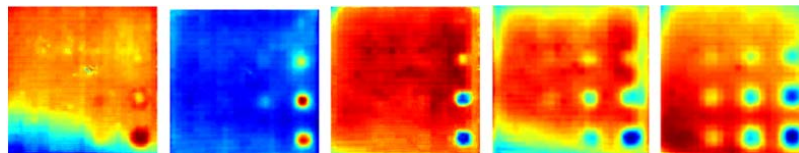
Figure 51: CFRP SNR of 2mm deep defect at 1500, 3000 and 6000 W

### 8.1.2 Experimental Results

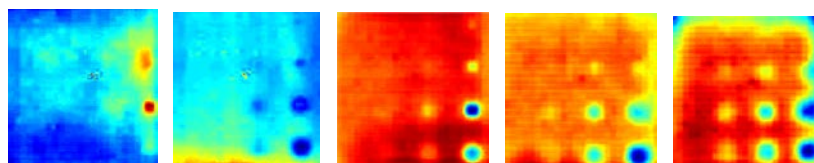
It was noted that high power promoted defect clarity. At 0.2 Hz, defects did not show distinctly in phasegrams obtained from experiments employing peak power intensity of 1500 W. This was attributed to the low surface temperature rise that produced a low thermal contrast between defects and the sound area. For a defect to be visible, the thermal contrast it causes must be sufficient enough to be detected by the infrared camera. An observation was made at 0.05 Hz when using 1500 and 6000 W of power, the 3 mm deep defects were visible at both intensities but not when using 3000 W that only revealed 2 mm deep defects. Lowering the frequency further, variation in lamp intensity had modest impact on the defect clarity as all three intensities produced similar results, showing similar defects at matched frequencies. Phase images obtained from experimental data at frequencies 0.2, 0.1, 0.05, 0.02 and 0.01 Hz for the three distinct heat intensities of 1500, 3000 and 6000 W are shown in Figure 52 a, b and c respectively.



(a) CFRP phase images with application of 1500 W



(b) CFRP phase images with application of 3000 W



(c) CFRP phase images with application of 6000 W

Figure 52: Experimental phase images for carbon fibre composite at 0.2, 0.1, 0.05, 0.02 and 0.01 Hz at varying intensities

### 8.1.2.1 Phase Contrast

The trends for the three intensities showed good correlation for the 2 mm deep defect, all having peak phase values at 0.02 Hz. The closeness of the values also suggests that the intensity of the excitation has little effect on defect detection except at high frequencies where high power is advantageous as it improves the thermal contrast between defective and nondefective regions. Further, the high power results in a significant temperature rise which minimises the effects of experimental noise. The phase response graph for the 2 mm deep defect is shown in Figure 53. For the deeper defects, there was not much difference among the three intensities in that they were only visible at low frequencies. This is evidenced in the phase image results of Figure 52 where the 3 mm and 4 mm deep defects only become visible at 0.02 Hz and 0.01 Hz and their contrast improved as the frequency was reduced from 0.02 Hz to 0.01 Hz.

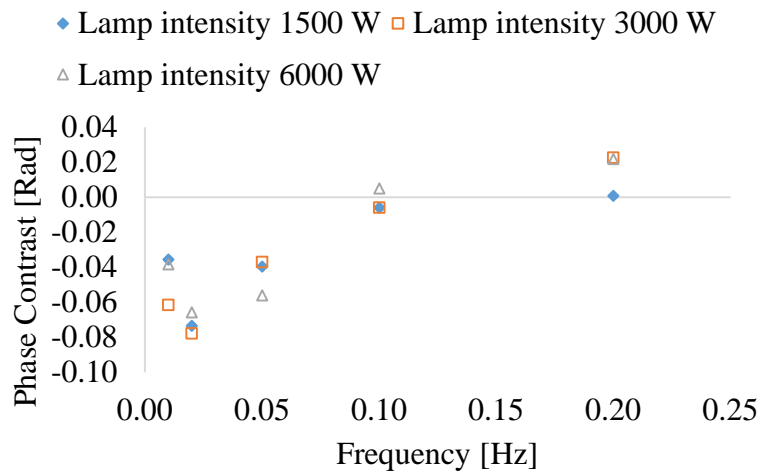


Figure 53: CFRP phase contrast comparison at 1500, 3000 and 6000 W excitation power

### 8.1.2.2 Signal-to-Noise-Ratio

At 6000 W, the 2 mm deep defect was visible for all frequencies used but the strength of the signal in comparison to its surrounding pixels varied. At high frequencies, the defect contrast was fairly high with high power which improved with reduction of excitation frequency and reached a maximum at 0.05 Hz. This was also the case with the intensity at 1500 W but using 3000 W yielded highest SNR at 0.1 Hz. It was observed that despite similar defects revealing at matched frequencies for all intensities, the SNR when using lamp power of 1500 W was

generally lower than when using 3000 W and 6000 W. The SNR plots for the 2 mm deep defect at 1500, 3000 and 6000 W are shown in Figure 54.

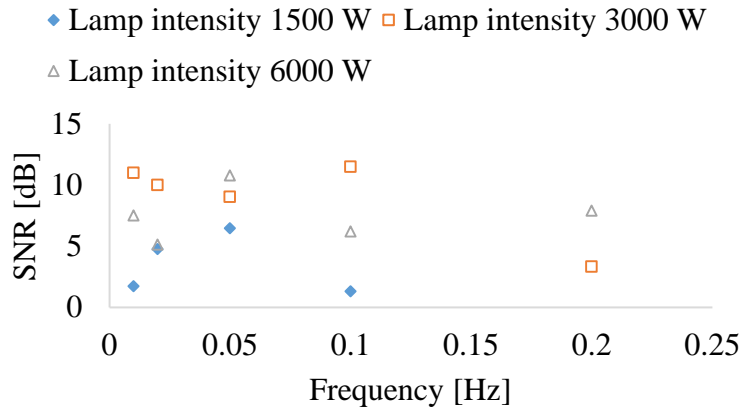


Figure 54: Experimental CFRP SNR for 2 mm deep defect at 1500, 3000 and 6000 W

## 8.2 Steel

### 8.2.1 Simulation Results

These showed slight variations in phase contrast results relating to defect clarity at all frequencies but 0.2 Hz. At this frequency, defect clarity for the 2 mm deep defect was significantly less for results obtained with an excitation intensity of 1500 W. All other frequencies produced similar images and defect representation. Simulation phase image results are shown in Figure 55.

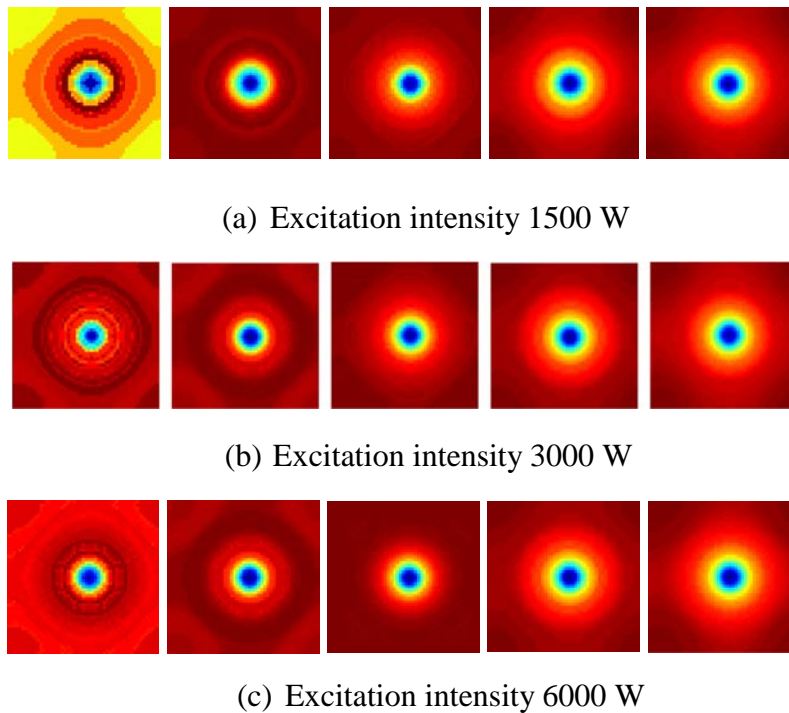


Figure 55: Steel phase images for 2 mm deep defect at 0.2, 0.1, 0.05, 0.02 and 0.01 Hz at varying excitation power intensities

### 8.2.1.1 Phase Contrast

The phase contrast values for the 2 mm deep defect had similar trends for all intensities and only varied by narrow margins. Simulation results notably showed an increment in overall temperature magnitude rise. The heat transfer mechanics in the simulations were similar due to less variation in heat capacity and thermal conductivity in steel. CFRP simulations showed higher overall temperature rises which affects the heat capacity and thermal conductivity as they are temperature dependant. Simulation phase contrast plots for the 2 mm deep defect at 1500, 3000 and 6000 W are shown in Figure 56.

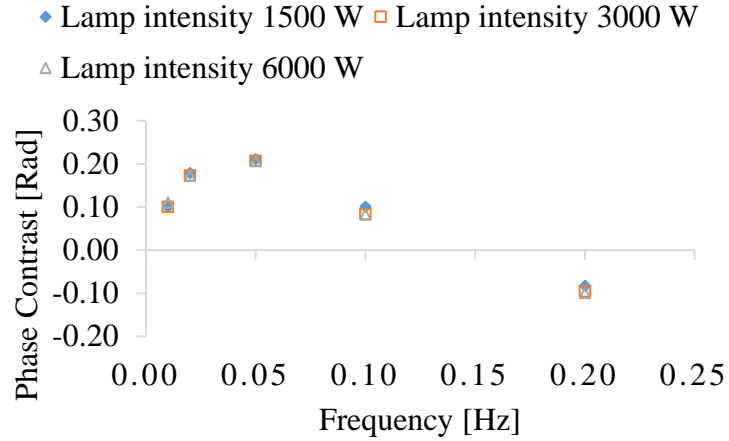


Figure 56: Phase contrast trend for 2 mm deep defect at varying intensities

### 8.2.1.2 Signal-to-Noise-Ratio

At 0.2 Hz, SNR values were fairly high at 3000 W and 6000 W and lowest at 1500 W. Lowering the frequency increased the SNR for simulations carried out at a lamp intensity of 1500 W to match with values obtained with 3000 W and 6000 W. That is, power intensity in steel simulation results also revealed that low power intensities significantly affected defect detection at high frequencies while at lower frequencies the effects were insignificant. SNR values for the 2 mm deep defect are shown in Figure 57.

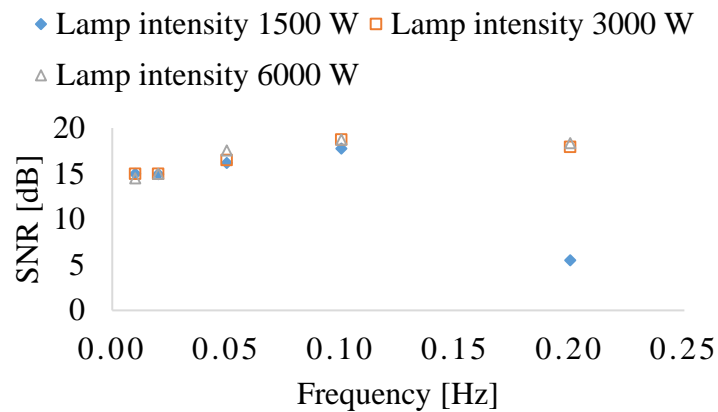
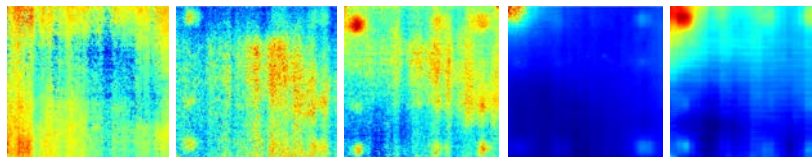


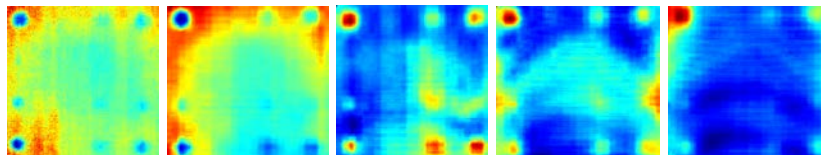
Figure 57: SNR for 2 mm deep defect at varying intensities

## 8.2.2 Experimental Results

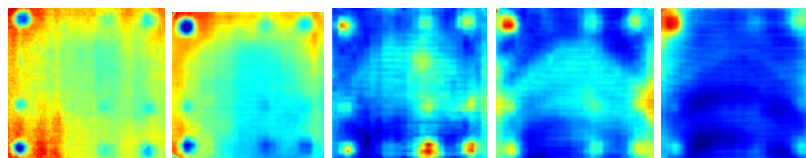
At 0.2 Hz, using an intensity of 1500 W produced noisy images of the surface temperature response. The noise appeared to lessen when the intensity of the excitation was raised to 3000 W and 6000 W. From 0.2 Hz to 0.05 Hz, phase images obtained from using an intensity of 1500 W contained visible noise and while those obtained from 3000 W and 6000 W showed the lowest amount of noise. Also, at 1500 W the fewest defects were detected and the ones detected showed weak signal strength. For intensities of 3000 W and 6000 W, defects detected were 10 mm and above at frequencies of 0.05 Hz to 0.02 Hz. At 0.2 Hz and 0.01 Hz, the fewest defects were detected. Low frequencies blurred the defect signatures which reduced their visibility on the phase images. Studies conducted earlier by Zimnoch *et al.*, 2010 proposed that excitation intensity above 2600 W aided in detecting defects with a diameter of 5 mm while Meola & Carlomagno, 2004 noted that local noise was high when surface temperature rise was low. Figure 58 shows phase images obtained at 0.2, 0.1, 0.05, 0.02 and 0.01 Hz with lamp intensities of 1500, 3000 and 6000 W.



(a) Steel phase images with application of 1500 W



(b) Steel phase images with application of 3000 W



(c) Steel phase images with application of 6000 W

Figure 58: Experimental phase images for steel at 0.2, 0.1, 0.05, 0.02 and 0.01 Hz for varying intensities

### 8.2.2.1 Phase Contrast

Phase contrast analysis was not conducted as only one out of the five frequencies used clearly revealed the defects. Rather, a temperature profile analysis was conducted at an excitation frequency of 0.2 Hz and a lamp power of 1500 W. Results shown in Figure 59 are the temperature response curve of the 10 mm deep defect exhibiting low overall temperature rise and a high level of noise. From the graph, results show that low surface temperature response signals are prone to noise degradation as the temperature measurement fluctuations are more pronounced. That is the effects of experimental noise are significantly higher which affects phase image results. Signal-to-noise-ratio analysis was not conducted as the results obtained did not clearly reveal the defects under study except for two at 0.05 Hz with lamp peak intensities of 3000 and 6000 W.

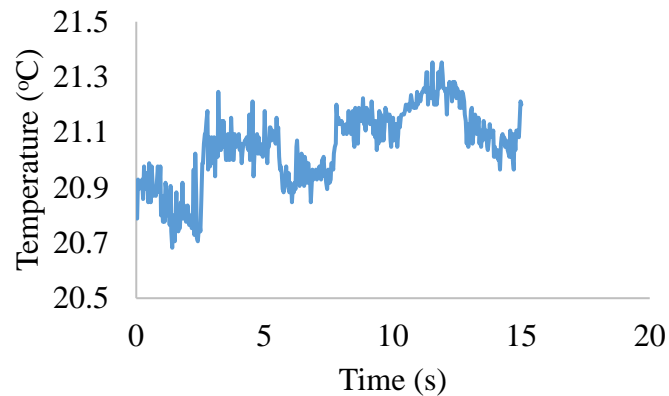


Figure 59: Surface temperature response for steel at 0.2 Hz with 1500 W excitation intensity

## 8.3 Chapter Summary

It was highlighted that excitation intensity in lockin thermography significantly affects phase image results. This is more pronounced at high frequencies in materials with high heat as the overall temperature rise is low. As a result of the low temperature rise, experimental noise significantly affected phase image results in that defects were not distinctly visible. The effect of experimental noise appeared to lessen as the frequency was lowered for both cases of CRFP and steel and the results obtained showed low variation. That is excitation power significantly affects results in materials of high heat capacity and in experiments conducted at high frequencies.

## 9 Discussion, Conclusion and Recommendations

### 9.1 Discussion

Nondestructive testing of composite materials is an integral part of construction, manufacturing, aviation and other industries to ensure that finished products can perform satisfactorily over their design life cycle. This study focused on lockin thermography for nondestructive testing of carbon fibre composite and mild steel samples to further understanding on factors that affect defect detectability. Four main parameters were investigated which were the excitation frequency, number of wave cycles and intensity and specimen material properties. To this end both simulations and experiments were conducted in order to better understand the effects of environmental factors on the capability of defect detection.

Results obtained from the study of frequency of thermal excitation indicated that the range of excitation frequencies chosen greatly affects the detection of deep defects. In materials with high thermal attenuation, the capability of defect detection rests upon selecting low excitation frequencies as they probe deeper into the material. In the surface temperature response to the excitation wave, results showed that the phase contrast of defects increased as the frequency of the wave was decreased which agrees with results obtained by Benny & Patty (1988) and Ibarra-Castenado (2004). The phase contrast curves obtained by Ibarra-Castenado (2004) are shown in Figure 60 showing the variation of phase contrast with frequency and defect depth. Having an increase in phase contrast was advantageous as it increased the probability of defect detection especially for the deeper defects that show very low phase contrast at high frequencies. This trend applied to both simulations and experimental data for all parameters investigated which were the number of thermal waves and intensity of excitation source and the material properties.

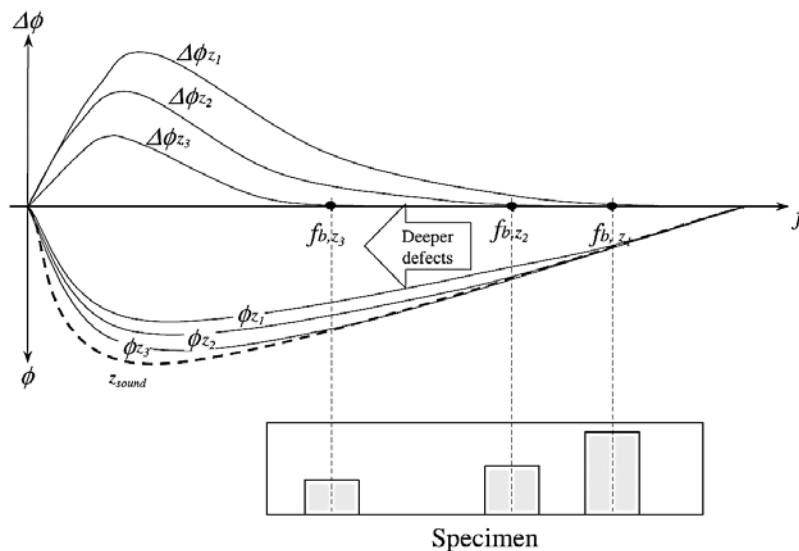


Figure 60: Variation of phase contrast with frequency (from Ibarra-Castanado *et al.*, 2004)

The number of excitation wave cycles also affected results where increasing the number of wave cycles increased defect clarity by reducing the effect of noise. This improvement was mostly in steel where using three excitation wave cycles produced noisy images at all frequencies in contrast to carbon fibre composite that produced comparable results between using three or five excitation wave cycles. At the lowest frequency of 0.01 Hz, defect SNR and phase contrast were appreciably low in CRFP when five excitation wave cycles were applied to the specimen surface which was attributed to high rate of lateral heat transfer due to the longer experimental time. In simulation data, the results were similar as environmental effects were absent and the models were symmetrical. Using five excitation wave cycles yielded improved results in experimental data for both steel and carbon fibre composites.

The excitation intensity affects defect detection as low intensities produce low temperature rises that are distorted by experimental noise. Too low a temperature rise resulted in the signal being indistinguishable from camera noise and hence poor image contrast. This was predominate in steel due to its high heat capacity that resulted in lower temperature rises for the same amount of heat deposited onto the sample surface as compared to carbon fibre composite that produced higher temperature rises. The effect of excitation intensity were more significant at higher frequencies in carbon fibre composite while low frequencies produced similar results showing similar defects at matched frequencies. In the case of steel, results obtained across all frequencies showed high dependence on excitation intensity as

the results obtained with an excitation intensity of 1500 W produced the worst results as smaller defects were not clearly distinct when compared with the larger ones.

Sample material properties also affected defect detectability as low thermal conductivity and heat capacity promoted defect clarity. Low thermal conductivity and heat capacity ensured good thermal contrast between defects and the sound regions which reduced the effect of experimental noise and lateral heat transfer on results.

In simulation data, most of the defects revealed due to the symmetry of the models and them having no experimental noise. This was particularly significant in steel experiments at high frequencies as they resulted in modest temperature rises that could not easily be distinguished between camera noise and signal. Frequency having a high significance on defect detection entails that in a sample of unknown defects, it is easier to predict defect location and size from frequency of excitation used.

## 9.2 Conclusion

Infrared thermography results vary vastly based on a number of factors including excitation frequency, number on wave cycles, excitation intensity and material properties. The influence each parameter had on defect detectability was investigated and the conclusions made are presented.

- i. The excitation frequency significantly affects defect detection low frequencies probing deeper into samples which agrees with findings of the majority of studies conducted on this parameter including Ranjit *et al.*, (2015).
- ii. The number of excitation wave cycles used is significant at high frequencies, using more excitation cycles aided in reduction of the influence of experimental noise on results and increased the SNR. This agrees with Duan *et al.*, (2013) who stated that increasing the number of excitation waves increased the SNR.
- iii. The intensity of thermal excitation affects materials with high heat capacity and thermal conductivity more due the low surface temperature rise produced which may match experimental noise when too low (Zimnoch *et al.*, 2010). These effects were more significant at higher frequencies.
- iv. Materials with high heat capacity and thermal conductivity are more challenging to detect defects using lockin thermography due the rapid heat propagation and low temperature rise requiring highly sensitive cameras to

effectively capture the low temperature rise and quick heat transfer processes occurring. This investigation was not contrasted against literature as the author was unable to obtain literature pertaining to contrasts between materials with a wide range of material property disparities.

### 9.3 Future Recommendations

Further investigations on image processing optimization would be beneficial so as to obtain maximum defect contrast in the image screen.

A modern infrared camera with high thermal resolution and low detector noise would be a good addition to studies aimed at understanding the full extent of deep defect detection using optical lockin thermography.

## References

- Adams. R.D & Cawley. P, 1988, “A Review of Defect Types and Nondestructive Testing Techniques for Composites and Bonded Joints”, *NDT International*, Vol. 21, No. 4, p. 208-222.
- Avdelidis. N.P, Almond. D.P, Dobbinson. A, Hawtin. B.C, Ibarra-Castanedo. C & Maldague. X, 2004, “Aircraft Composites Assessment by Means of Transient Thermal NDT”, *Progress in Aerospace Sciences*, Vol. 40, p. 143-162.
- Aymerich. F & Meili. S, 1999, “Ultrasonic Evaluation of Matrix Damage in Impacted Composite Laminates”, *Composites: Part B*, Vol. 31, p. 1-6.
- Bates. D, Smith. G, Lu. D & Hewitt. J, 2000, “Rapid Thermal Nondestructive Testing of Aircraft Components”, *Composites: Part B*, Vol. 31, p. 175-185.
- Breitenstein. O, Warta. W & Langenkamp. M, 2010, “Lockin Thermography”, Springer.
- Cantwell. W.J & Morton. J, 1992, “The Significance of Damage and Defects and their Detection in Composite Materials: A Review”, *Journal of Stain Analysis*, Vol. 27, No. 1, p. 29-42.
- Cawley. P, 1984, “The Impedance Method of Nondestructive Inspection”, *NDT International*, Vol. 17.
- Chatterjee. K, Tuli. S, Pickering . S.G & Almod. D.P, 2011, “A Comparison of the Pulsed, Lockin and Frequency Modulated Thermography Nondestructive Evaluation Techniques”, *NDT&E International*, Vol. 44, p. 655-667.
- Chatterjee. K & Tuli. S, 2013, “Prediction of Blind Frequency in Lockin Thermography Using Electro-Thermal Model Based Numerical Simulation”, *Journal of Applied Physics*, Vol. 114.
- Choi. M, Kang. K, Park. J, Kim. W & Kim. K, 2008, “Quantitative Determination of a Subsurface Defect of Reference Specimen by Lockin Infrared Thermography”, *NDT&E International*. Vol. 41, p. 119-124.
- Duan. Y, Huebner. S, Hassler. U, Osman. A, Ibarra-Castanedo. C & Maldague. X.P, 2013, “Quantitive Evaluation of Optical Lockin and Pulsed Thermography for Aluminium Foam Material”, *Infrared Physics and Technology*, Vol. 60, p. 275-280.
- du Plessis. A, le Roux. S.G & Guelpa. A, 2016, “The CT scanner Facility at Stellenbosch University: An open access X-ray Computed Tomography Laboratory”, *Nuclear Instruments and Methods in Physics Research: Part B*, Vol. 384, p. 42-49.
- FLIR systems, 2016. FLIR camera calibration technical data. Available [Online]: <http://www.flir.com/instruments/display/?id=59962>. (Accessed 15 August 2016).

- Gao. S.L & Kim. J.K, 1999, "Scanning Acoustic Microscopy as a Tool for Quantitative Characterization of damage in CFRPs", *Composites Science and Technology*, Vol. 59, p. 345-354.
- Ghali. V.S, Mulaveesala. R & Takei. M, 2011, "Frequency-Modulated Thermal Wave Imaging for Nondestructive Testing of Carbon Fibre-Reinforced Plastic Materials", *Measurement Science and Technology*, Vol. 22.
- Griffith. B, Törlér. D & Goudey. H, 2001, "Infrared Thermographic Systems: A Review of IR Imagers and their Use", *Encyclopedia of Imaging Science and Technology*, John Wiley and Sons Inc, New York.
- Hidalgo-Gato. R, Andrés. J.R, López-Higuera. J.M & Madruga. F.J, 2013, "Quantification by Signal to Noise Ratio of Active Infrared Thermography Data Processing Techniques", *Optics and Photonics Journal*, Vol. 3, p. 20-26.
- Hung. Y.Y, 1996, "Shearography for Nondestructive Evaluation of Composite Structures", *Optics and Lasers in Engineering*. Vol. 24, p. 161-182.
- Ibarra-Castanedo. C, González. D, Klein. M, Pilla. M, Vallerand. S & Maldague. X.P, 2004, "Infrared Image Processing and Data Analysis", *Infrared Physics and Technology*, Vol. 46, p. 75-83.
- Ibarra-Castanedo. C, 2005," Quantitative Subsurface Defect Evaluation by Pulsed Phase Thermography: Depth Retrieval with the Phase", Ph. D Thesis, Laval University.
- Ibarra-Castanedo. C, Piau. J.C, Guilbert. S, Avdelidis. N.P, Genest. M, Bendada. A & Maldague. X.P, 2009, "Comparative Study of Active Thermography Techniques for the Nondestructive Evaluation of Honeycomb Structures", *Research in Nondestructive Evaluation*, Vol. 20, p. 1-31.
- Ibarra-Castanedo. C, Tarpani. J.R & Maldague. X.P, 2013, "Nondestructive Testing with Thermography", *European Journal of Physics*, Vol. 34, p. 91-109.
- Joven. R, Das. R, Ahmed. A, Roozbehjavan. B & Minaie. B, 2012, "Thermal Properties of Carbon Fiber-Epoxy Composites with Different Fabric Weaves", *SAMPE International Symposium Proceedings*.
- Junyan. L, Liqiang. L & Yang. W, 2013, "Experimental Study on Active Thermography as a NDI Tool for Carbon-Carbon Composites", *Composites Part: B*, Vol. 45, p. 138-147.
- Junyan. L, Yang. L, Fei. W & Yang. W, 2015, "Study on Probability of Detection (POD) Determination Using Lockin Thermography for Nondestructive Inspection (NDI) of CFRP Composite Materials", *Infrared Physics and Technology*, Vol. 71, p. 448-456.
- Kalogiannakis. G, van Hemelrijck. D & van Assche. G, 2004, "Measurements of Thermal Properties of Carbon/Epoxy and Glass/Epoxy using Modulated Temperature Differential Scanning Calorimetry", *Journal of Composite Materials*, Vol. 38. No. 2.

- Krapez. J.C, Pacou. D & Gardette. G, 2000, “Lockin Thermography and Fatigue Limit of Metals”, Office National D Etudes et de Recherches Aersospaciales Onera.
- Kretzmann. J.E, 2016, “Evaluating the Industrial Applllication of Nondestructive Inspection of Composites using Transient Thermography”, Masters Thesis, Stellenbosch University.
- Krumm. M, Sauerwein. C, Hämmerle. V, Oster.R, Diewel. B, Sindel. M & Audi. A.G, 2012, “Capabilities and Appllication of Specialized Computed Tomography Methods for the Determination of Characteristic Material Properties for Fibre Composite Components”, Conference on Industrial Computed Tomography, p. 19-21.
- Lahiri. B.B, Bagavathiappan. S, Reshmi. P.R, Philip. J, Jayakumar. T & Raj. B, 2012, “Quantification of Defects in Composites and Rubber Materials Using Active Thermography”, Infrared Physics and Technology, Vol. 55, p. 191-199.
- MatWeb Material Property Data, 2016. AISI 1015 Steel. Available [Online]: <http://www.matweb.com/search/DataSheet.aspx?MatGUID=6cd3ff8c19bb42bda1fa848e6d12bbb9> (Accessed 10 July 2016).
- Meola. C, Carlomagno. G.M & Giorleo. L, 2004, “The Use of Infrared Thermography for Materials Characterization”, Journal of Materials Processing Technology, p. 1132-1137.
- Meola. C & Carlomagno. G.M, 2004, “Review Article: Recent Advances in the Use of Infrared Thermography”, Measurement Science and Technology, Vol. 15, p. 27-58.
- Meola. C, Carlomagno. G.M & Giorleo. L, 2004, “Geometrical Limitations to Detection of Defects in Composites by Means of Infrared Thermography”, Journal of Nondestructive Evaluation, Vol. 23, No. 4, p. 125-132.
- Meola. C, Carlomagno. G.M, Squillace. A & Giorleo. G, 2004, “The Use of Infrared Thermography for Nondestructive Evaluation of Joints”, Infrared Physics and Technology, Vol. 46, p. 93-99.
- Meola. C, Grasso. V, Toscano. C & Carlomagno. G.M, 2013, “Nondestructive Testing of Fibre Reinforced Polymers with Lockin Thermography”, Residual Stress, Thermomechanics and Infrared Imaging, Hybrid Techniques and Inverse Problems, Vol. 8, p. 207-213.
- Peng. D & Jones. R, 2013, “Modelling of the Lockin Thermography Process through Finite Element Method for Estimating the Rail Squat Defects”, Engineering Failure Analysis, Vol. 28, p. 275-288.
- Pitaressi. G, 2012, “Implementation of a Fast and Low Cost IR-NDT Technique by Means of a Square Pulse Modulated Lockin Thermography”, 11<sup>th</sup> International Conference on Quantitative Infrared Thermography.

- Pitaressi. G, 2015, "Lockin Signal Post-Processing Techniques in Infrared Thermography for Materials Structural Evaluation", *Experimental Mechanics*, Vol. 55, p. 667-680.
- Ranjit. S, Kang. K and Kim. W, 2015, "Investigation of Lockin Infrared Thermography for Evaluation of Subsurface Defects Size and Depth", *International Journal of Precision Engineering and Manufacturing*, Vol. 16, No. 11, p. 2255-2264.
- Riegert. G, Pfleiderer. K, Gerhard. H, Solodov. I & Busse. G, 2006, "Modern Methods of NDT for Inspection of Aerospace Structures", *ECNDT-We.4.1.4*.
- Rogalski. A, 2003, "Infrared Detectors: Status and Trends", *Progress in Quantum Detectors*, Vol. 27, p. 59-210.
- Rogalski. A, 2012, "Progress in Focal Plane Array Technologies", *Progress in Quantum Physics Electronics*, Vol. 36, p. 342-473.
- Schwartz. M, 2002, "Encyclopedia of Materials, Parts and Finishes".
- Scott I.G & Scala C.M, 1982, "A Review of Non-Destructive Testing of Composite Materials", *NDT International*.
- Servias. P & Gerlach. N, 2006, "Development of a New NDT Method Using Thermography for Composite Inspection On Aircraft With Portable Military Thermal Imager" *Vth International Workshop, Advances in Signal Processing for Nondestructive Evaluation of Materials*.
- Sharath. D, Menaka. M & Venkatraman. B, 2013, "Effect of Defect Size on Defect Quantification in Pulsed Thermography", *Measurement Science and Technology*, Vol. 24, p. 1-7.
- Steiner. K.V, Eduljee. R.F, Huang. X & Gillespie. J.W.Jr, 1995, "Ultrasonic NDE Techniques for the Evaluation of Matrix Cracking in Composite Laminates", *Composites Science and Technology*, Vol. 53, p. 193-198.
- Susa. M, Benítez. H.D, Ibarra-Castanedo. C, Loaiza. H, Bendada. H & Maldague. X, 2006, "Phase Contrast Using a Differentiated Absolute Contrast Method", *Quantitative Infrared Thermography*, No. 3, Vol. 2, p. 219-230.
- Sweeting. R.D & Liu. X.L, 2004, "Measurement of Thermal Conductivity for Fibre-Reinforced Composites", *Composites: Part A*, Vol. 35, p. 933-938.
- Wallbrink. C, Wade. S.A & Jones. R, 2007, "The Effect of Size on the Quantitative Estimation of Defect Depth in Steel Structures Using Lockin Thermography", *Journal of Applied Physics*, Vol. 101, p. 1-8.
- Wevers. M, 1997, "Listening to the Sound of Materials: Acoustic Emission for the Analysis of Material Behaviour", *NDT&E International*, Vol. 30. No. 2, p. 99-106.
- Wilcox. M & Downes. G, 2003, "A Brief Description of NDT Techniques", Toronto: NDT Equipment Ltd.

Zimnoch. M, Oliferuk. W & Maj. M, 2010, “Estimation of Defect Depth in Steel Plate Using Lockin Infrared Thermography”, *Acta Mechanica et Automatic*, Vol. 4, No. 4, p. 106-109.

Zoecke. C, Langmeier. A & Arnold, 2010, “Size Retrieval of Defects in Composite Material with Lockin Thermography”, *Journal of Physics*, Vol. 214, p. 1-5.

## Appendix A Sample Dimensions

### A.1 Introduction

Sample drawings are presented showing the positions of the inserted defects. Both carbon fibre and steel are presented together with their dimensions. They were developed using Autodesk Inventor 2016.

### A.2 Carbon Fibre Sample Dimensions

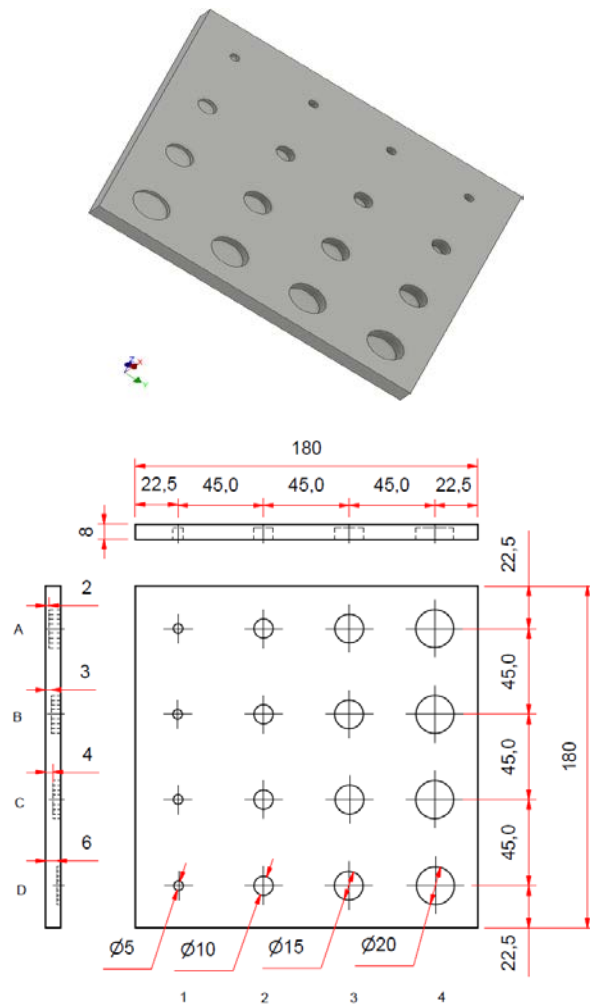


Figure 61: Carbon fibre sample dimensions and defect layout

Table 5: Defect Dimensions and depth for carbon fibre sample

Hole Number	Diameter (mm)	Depth (mm)
A <sub>1</sub>	5	2
A <sub>2</sub>	10	2
A <sub>3</sub>	15	2
A <sub>4</sub>	20	2
B <sub>1</sub>	5	3
B <sub>2</sub>	10	3
B <sub>3</sub>	15	3
B <sub>4</sub>	20	3
C <sub>1</sub>	5	4
C <sub>2</sub>	10	4
C <sub>3</sub>	15	4
C <sub>4</sub>	20	4
D <sub>1</sub>	5	6
D <sub>2</sub>	10	6
D <sub>3</sub>	15	6
D <sub>4</sub>	20	6

### A.3 Steel Sample Dimensions

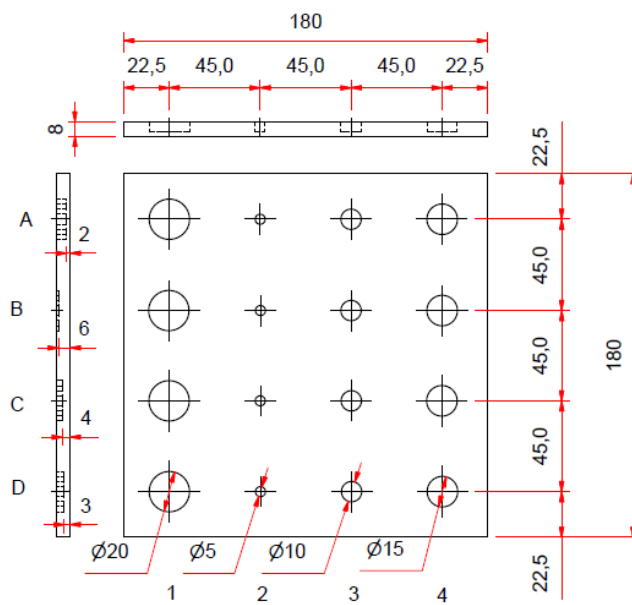
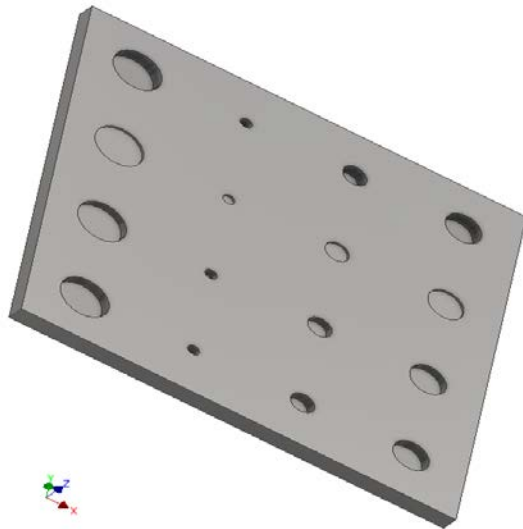


Figure 62: Steel sample dimensions and defect layout

Table 6: Defect Dimensions and depth for steel sample

Hole Number	Diameter (mm)	Depth (mm)
A <sub>1</sub>	20	2
A <sub>2</sub>	5	2
A <sub>3</sub>	10	2
A <sub>4</sub>	15	2
B <sub>1</sub>	20	6
B <sub>2</sub>	5	6
B <sub>3</sub>	10	6
B <sub>4</sub>	15	6
C <sub>1</sub>	20	4
C <sub>2</sub>	5	4
C <sub>3</sub>	10	4
C <sub>4</sub>	15	4
D <sub>1</sub>	20	3
D <sub>2</sub>	5	3
D <sub>3</sub>	10	3
D <sub>4</sub>	15	3

## Appendix B Infrared Basics

### B.1 Infrared Radiation

All objects above 0 K (-273 °C) emit infrared radiation. Infrared radiation that consists of electromagnetic waves in the spectral band between microwave and visible light that is from 0.75  $\mu\text{m}$  to 1000  $\mu\text{m}$ . The infrared spectrum is subdivided in the near infrared (0.76 – 1.5  $\mu\text{m}$ ), medium infrared (1.5 – 5.6  $\mu\text{m}$ ) and far infrared (5.6 – 1000  $\mu\text{m}$ ). Figure 62 shows the position of infrared radiation on the electromagnetic spectrum.

**Figure 1: Infrared Region of Electromagnetic Spectrum**

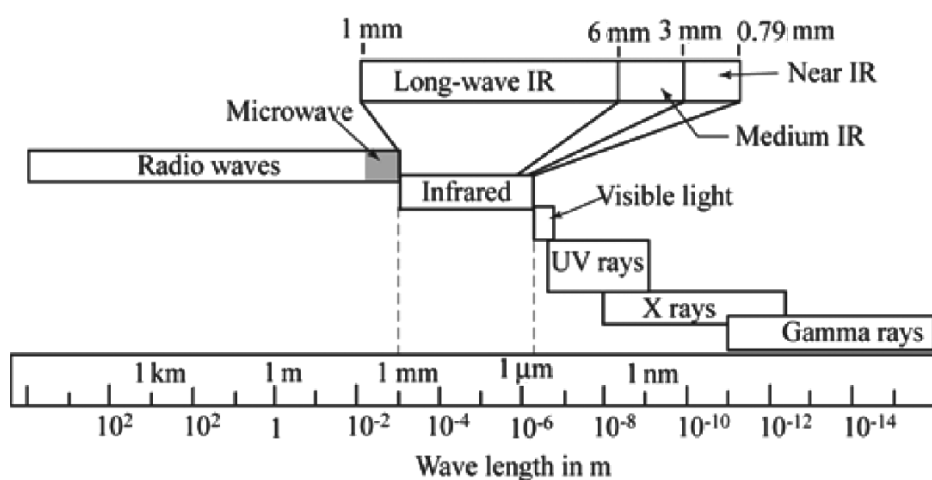


Figure 63: Infrared radiation on the electromagnetic spectrum (from Sultan *et al.*, 2012)

### B.2 Infrared Transmission Media

Infrared radiation can be transmitted through a vacuum, atmosphere and optical fibres. The amount of radiation transmitted by these media varies and is of importance to get acquainted with the absorption through atmosphere for remote sensing. There are a variety of particles in the atmosphere that absorb infrared radiation of varying wavelengths. Of interest are the wavelengths where maximum

transmission occurs referred to as atmospheric windows. These windows are from 3 – 5  $\mu\text{m}$  and 8 – 14  $\mu\text{m}$  and detectors have been developed which have highest sensitivity in these transmission windows. Figure 64 below shows the atmospheric windows that transmit the most amount of radiation.

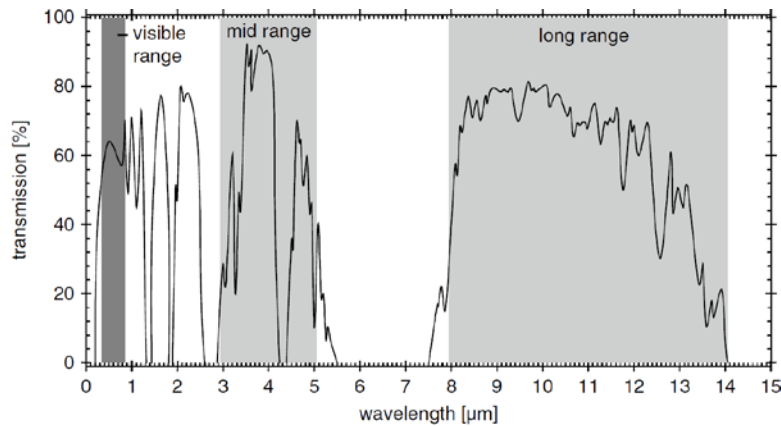


Figure 64: Infrared transmission window

### B.3 Infrared Thermography Approaches

Infrared thermography is broadly classified either as active or passive. In the passive approach, no stimulus is applied to the specimen as the thermal contrast between defective and nondefective parts is sufficient to detect internal flaws. In most cases, this method is used when the specimen is not at ambient temperature. Some industry applications of this technique are in predictive maintenance, inspection of thermal insulation and quality control. In the active approach, a stimulus is applied to the specimen to create thermal contrast between defective and nondefective samples. The presence of an inhomogeneity in the tested material affects the heat movement and produces local surface temperature distributions. This method is widely used for NDE of material for flaws.